Wenchao Du
Department of Industrial and Systems Engineering,
Texas A&M University,
College Station, TX 77843
e-mail: wenchaodu@tamu.edu

Xiaorui Ren
Department of Mechanical Engineering,
Texas A&M University,
College Station, TX 77843
e-mail: renxiaorui@tamu.edu

Zhijian Pei
Department of Industrial and Systems Engineering,
Texas A&M University,
College Station, TX 77843
e-mail: zjpei@tamu.edu

Chao Ma[1]
Department of Engineering Technology and Industrial Distribution;
Department of Industrial and Systems Engineering;
Department of Mechanical Engineering,
Texas A&M University,
College Station, TX 77843
e-mail: cma@tamu.edu

Ceramic Binder Jetting Additive Manufacturing: A Literature Review on Density

The objective of this review paper is to summarize the current status and identify the knowledge gaps in ceramic binder jetting additive manufacturing, with a particular focus on density. This paper begins with an overview of ceramic binder jetting. Then, it discusses different aspects of density, including various terminologies, measurement methods, and achieved values. Afterward, it reviews two categories of techniques to increase the part density: material preparation techniques (powder granulation, mixing powders of different sizes, using slurry feedstock, and mixing different materials) and postprocessing techniques (sintering, chemical reaction, infiltration, and isostatic pressing). Finally, it presents the knowledge gaps in the literature. [DOI: 10.1115/1.4046248]

1 Introduction

Ceramic materials can have outstanding properties, such as extraordinary hardness, excellent resistance to wear, heat, and corrosion, and exceptional biocompatibility. Therefore, ceramic materials have a wide range of applications, from orthopedic and dental implants in the biomedical industry to engine components in the aerospace and automotive industries. However, it is very costly to fabricate ceramic parts of complex shapes using conventional manufacturing techniques. For complex ceramic parts, tooling can contribute up to 80% of the overall cost if conventional techniques are used [1]. Conventional techniques have other disadvantages including excessive cost in prototyping and difficulty to make design changes. All these disadvantages have impeded the widespread applications of advanced ceramic materials (e.g., alumina, zirconia, and silicon carbide). For example, there are millions of joint replacement surgeries every year [2]. Although ceramic materials are an excellent choice for joint implants because of their excellent wear resistance and exceptional biocompatibility [3], they are not widely utilized because it is not cost-effective to fabricate them using conventional manufacturing technologies [4].

According to the ASTM standard [5], most additive manufacturing (AM) technologies can be classified into seven categories: binder jetting, vat photopolymerization, powder bed fusion, directed energy deposition, material extrusion, material jetting, and sheet lamination. Binder jetting is defined by ASTM as "additive manufacturing processes in which a liquid bonding agent is selectively deposited to join powder materials" [5]. Binder jetting was initially developed at Massachusetts Institute of Technology in the late 1980s [6,7] and commercialized by Soligen in 1993 [8], Z Corporation [9] and Therics [10] in 1997, ExOne in 2001 [11], Voxeljet in 2002 [12], Microjet in 2016 [13], and Desktop Metal [14] and Digital Metal [15] in 2017. After presenting their innovation in various conference [7,16,17] and journal [18,19] papers, the inventors investigated different perspectives of this technology, including the powder bed density improvement [20,21], powder–binder interaction [22,23], new feedstock form (i.e., slurry instead of powder) [24–31], and potential application areas (e.g., casting cores and shells [32], optical lenses [29], cutting tools [33], and biomedical devices [34]).

Table 1 summarizes advantages and disadvantages of the seven AM categories for printing ceramic materials. Compared with others, binder jetting has some unique features. First, the surrounding powder supports the printed part during the building process. Therefore, there is no need for explicit support structures for overhangs and undercuts [35]. Second, the amount of binder in the green body is low, and thus debinding is much easier for large parts than some other processes such as vat photopolymerization [36,43]. Third, as print heads can consist of up to thousands of jets working in parallel, binder jetting is easily scalable for fabricating large parts [37]. Moreover, binder jetting is suitable for biomedical applications due to its capability of printing functionally graded materials [44]. For example, bioinks with drugs can be added to the binder [45].

Several review papers on ceramic AM have discussed binder jetting. The first paper [46], which was published in 2003, discussed its process, dimensional control, and applications. Other four ceramic AM review papers, published in 2014 [39,47], 2015 [38], and 2017 [48], also included binder jetting. Travitzky et al. [39] reviewed the dimensional control methods and several applications in the orthopedic field. Deckers et al. [47] reviewed the low-density issue of ceramic binder jetting. Zocca et al. [38] reviewed the material preparation methods to improve the powder bed density, while Yang and Miyanaji [48] discussed the advantages and material limitations of ceramic binder jetting. A recent review paper about binder jetting summarized various powder deposition methods, reviewed binder selection criteria, and discussed key printing parameters such as binder saturation and layer thickness [49].

[1]Corresponding author.

Manuscript received September 25, 2018; final manuscript received January 30, 2020; published online February 5, 2020. Assoc. Editor: Kevin Chou.

Table 1 Advantages and disadvantages of various AM categories for ceramics

Category	Advantage	Disadvantage
Binder jetting	No need for support [35], minimal amount of sacrificial materials [36], high scalability [37]	High porosity [38]
Vat photopolymerization	Excellent accuracy [39], smooth surface [39], high density [38]	Limited part size
Powder bed fusion (indirect)	No need for support	High porosity
Material extrusion	Low cost, high density, multiple materials within a part [40]	Low accuracy [38], interfacial porosity
Material jetting	Smooth surface [39], multiple materials within a part	Limited part size
Directed energy deposition	High density [41]	Thermal cracks [42]
Sheet lamination	High speed, no need for support	Delamination, interfacial porosity [38]

In addition to these review papers, a book chapter also reviewed some ceramic materials that had been used in binder jetting, including several applications related to these materials [50].

The literature is receiving an increasing number of studies on binder jetting. Various techniques have been reported to improve the density (and mechanical properties in some cases) of printed parts. However, there are no review papers devoted to ceramic binder jetting that comprehensively compile the available reports in the literature on density improvement. This literature review is to fill the gap.

This paper first provides an overview of ceramic binder jetting, including the process, materials, and resultant densities. The focus of this review is to summarize and analyze reported techniques for density improvement, which is considered as the most challenging issue in this field. Finally, existing knowledge gaps are identified.

2 Description of Ceramic Binder Jetting

2.1 Process Overview. Figure 1 illustrates major components of a binder jetting 3D printer, including powder stock, build platform, spreader, binder cartridge, and print head. The printing process is as follows. First, the spreader deposits a thin layer of powder from the powder stock onto the build platform, forming the powder bed. Then, the print head jets binder onto selected areas defined by a 3D model to bond the powder particles in these areas. After one layer is finished, the build platform is lowered and the powder stock is raised, after which a new powder layer is spread onto the finished layer. These steps are repeated until the whole part is printed. The printed part is then separated from the loose powder after curing [6,36].

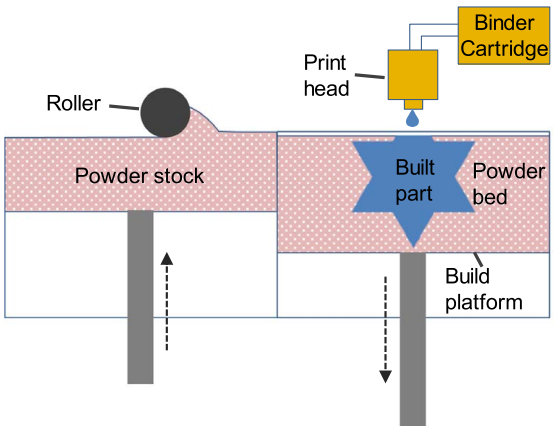

Fig. 1 Major components of a binder jetting 3D printer

A generic cycle of ceramic binder jetting is shown in Fig. 2. The feedstock is ceramic powder. The powder needs to meet certain requirements (e.g., high flowability and sinterability is discussed in Sec. 2.3) for making high-quality parts. The printed part is called "green part." The green part is then heated to a specific temperature (usually around 200 °C), during which the binder is thermally activated by solvent evaporation, polymerization, cross-linking, or other mechanisms to strengthen the green part [39,47]. It should be noted that curing can be applied layer by layer [51]. Curing temperature could be higher (up to 800 °C) if inorganic binder, usually colloidal silica [18], is used.

Afterward, postprocessing steps (such as debinding and sintering) are usually applied to the green parts to improve their material properties. In the debinding step, the binder is thermally decomposed or burned out by heat treatment between 400 °C and 800 °C, producing a "brown part." The heating rate is controlled to ensure the escape of gaseous reaction products. In the sintering step, the part is heated to a high temperature (usually just below the melting point of the ceramic material), followed by dwelling and furnace cooling. The sintering step increases the density of the part by mass transport across the boundaries of ceramic particles [52]. Other densification techniques (e.g., isostatic pressing, infiltration) can also be used to further increase the density and thus mechanical properties. However, they may compromise other properties such as geometrical accuracy, biocompatibility, and heat resistance. Details of some postprocessing steps are reviewed in Sec. 5.

2.2 Materials and Applications. Figure 3 shows the proportions of application areas of ceramic binder jetting in reported studies. The application with the highest number of papers is in the orthopedic field to make bone scaffolds and implants. The structural

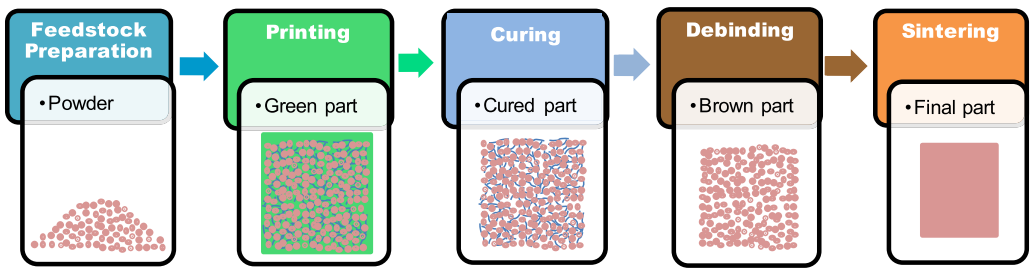

Fig. 2 Steps of ceramic binder jetting

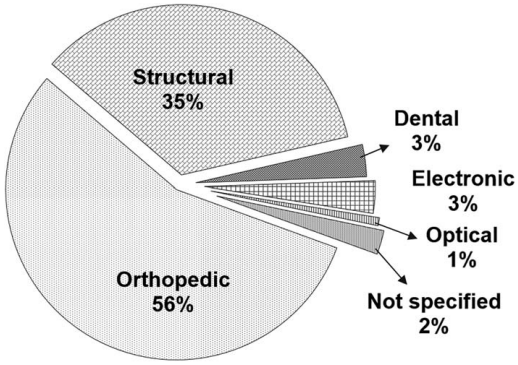

Fig. 3 Proportions of various application areas of ceramic binder jetting reported in the literature

application has the second highest number of papers. A small number of dentures and crowns are reported as well. For electronic applications, fabrication of dielectric radio frequency filters and ferroelectric dielectric capacitors is reported. There is also one paper about the fabrication of a gradient-index lens for optical application.

Table 2 summarizes the reported materials grouped by their application areas. Sometimes, the feedstock and resultant materials (if identified) are different and thus listed in different columns. Additives and infiltrants are also included.

Materials investigated for structural applications include oxides (Al_2O_3, TiO_2, and ZrO_2), carbides (WC, TiC, and SiC), and nitrides (AlN and Si_3N_4). For orthopedic applications, materials in the calcium phosphate family, such as hydroxyapatite ($Ca_5(PO4)_{3-}(OH)$) and tricalcium phosphate ($Ca_3(PO_4)_2$), are the most common choice due to their compositional similarity to human bones and thus excellent biocompatibility [177]. Other calcium phosphate materials include calcium polyphosphate ($[Ca(PO_3)_2]_n$), tetracalcium phosphate ($Ca_4(PO_4)_2O$), and dicalcium phosphate ($CaHPO_4$). Alumina is the first material studied by the inventors of binder jetting [6,7]. In the past decades, it is also one of the mostly studied materials in different applications including structural, electronic, and dental areas.

In addition to the pure compound materials, a large portion of studies used composites to enhance various properties. For example, 12.5 vol% zirconia was mixed with 40 vol% alumina slurry to attain optimum strength for the printed and sintered parts [72]. Although composite materials can offer improved properties, they sometimes sacrifice other properties such as biocompatibility [36].

2.3 Feedstock Powder. Feedstock powder and its deposition method determine various physical and chemical processes during fabrication, such as powder spreading, binder–powder interaction, and sintering densification [178]. This section discusses important feedstock powder parameters and deposition methods.

2.3.1 Powder Flowability. Flowability, the ability of a powder to freely flow, is crucial for uniform powder spreading [179] and thus homogeneous green and sintered part structure [48]. Flowability [103,170] is also called depositability [180], mobility [59], pourability [39], and spreadability [69,75,112,172].

Flowability can be assessed using different metrics, including the flow factor (ff_c) [111,112], the Hausner ratio (HR) [11,40,79–81], the Carr index (CI) [151], and the flow rate [149,153,155], among others. The flow factor is defined by the following equation:

$$ff_c = \frac{\sigma_1}{\sigma_c} \tag{1}$$

where σ_1 is the consolidation stress and σ_c is the compression strength, both of which can be measured with a ring shear tester [111,112].

The Hausner ratio [11,40,79–81] is defined by the following equation:

$$HR = \frac{\rho_t}{\rho_a} \tag{2}$$

where ρ_t and ρ_a are the tap density (the density of powder after a certain number of tapping cycles [64,98,181,182]) and the apparent density (the density of freely settled powder), respectively. HR value is always larger than or equal to one. A smaller HR value, i.e., closer to one, indicates better flowability. The Carr index [151] is similar to the Hausner ratio. A smaller index value indicates better flowability. Its definition and relationship with the Hausner ratio are shown as follows:

$$CI = 100\left(1 - \frac{\rho_a}{\rho_t}\right) \tag{3}$$

$$CI = 100\left(1 - \frac{1}{HR}\right) \tag{4}$$

The flow rate is usually measured by a Hall flowmeter [149,153,155], in which a defined volume of powder passes through a small opening of a metal funnel. The flow rate can be represented by the total time required for a certain amount of powder to pass [92,153] or the mass of the powder passing through in a unit time [149,155].

2.3.2 Powder Sinterability. Sintering is "a thermal treatment for bonding particles into a coherent, predominantly solid structure via mass transport events that often occur on the atomic scale" [183]. It is affected by powder properties and packing state. Powder sinterability is used to compare the sintering performance of different powders under a similar packing condition, and it is important for the selection of the optimal feedstock material before printing. Sintered bulk density is commonly used to describe powder sinterability since high sinterability leads to high sintered density under same conditions [52]. Volumetric shrinkage is another sinterability metric because high sinterability leads to large volumetric shrinkage under same conditions [184]. Powder sinterability can also be assessed by the densification ratio:

$$\varphi = \frac{\rho_s - \rho_g}{\rho_{th} - \rho_g} \tag{5}$$

where φ is the densification ratio and ρ_g, ρ_s, and ρ_{th} are the green density, sintered density, and theoretical density, respectively [185]. Theoretical density is calculated based on the corresponding crystal structure [186].

2.3.3 Powder Particle Shape. Various particle shapes have been reported in the literature, as shown in Fig. 4. Spherical particles usually have better flowability. For example, the flow times of spherical and irregular calcium alkaline phosphate powders (45–90 μm, 50 g) are 121 and 166 s under same conditions, respectively [106], which indicates the better flowability of spherical particles.

There are no reported studies about effects of powder particle shape in ceramic binder jetting. However, effects of particle shape on powder bed density were reported from other fields, such as geology [187]. Compared with nonspherical powders, sand powder with spherical particle shape could lead to a higher value of powder bed density [187].

2.3.4 Powder Particle Size. The reported particle size of the feedstock powder used in ceramic binder jetting ranges from 0.3 (the minimum particle size in Ref. [173]) to 355 μm (the maximum particle size in Ref. [167]). The particle size of the feedstock powder in binder jetting affects powder flowing and sintering behaviors.

Table 2 Feedstock and resultant materials in reported studies on ceramic binder jetting

Application	Feedstock material	Additive (A) or infiltrant (I)	Resultant material	Reference
Structural	Al	–	Al_2O_3	[53]
Structural	$Al + Al_2O_3$	–	Al_2O_3	[54]
Structural	AlN	–	AlN	[55,56]
Structural	Al_2O_3	–	Al_2O_3	[7,18,19,23,24,37,57–68]
Structural	Al_2O_3	(I) Al_2O_3	Al_2O_3	[69]
Structural	Al_2O_3	(I) $Cu + Cu_2O$	$Al_2O_3 + Cu + Cu_2O$	[67,70]
Structural	Al_2O_3	(I) Glass	Al_2O_3 + glass	[71]
Structural	$Al_2O_3 + ZrO_2$	–	$Al_2O_3 + ZrO_2$	[72]
Structural	$B_4C + SiC$	–	$B_4C + SiC$	[73]
Structural	CaO	(A) ZrO_2	$CaO + CaZrO_3$	[74]
Structural	$CaSO_4{\cdot}0.5H_2O$	–	$CaSO_4{\cdot}0.5H_2O$	[75]
Structural	$CaSO_4{\cdot}0.5H_2O$	(I) $C_{21}H_{25}ClO_5$	$C_{21}H_{25}ClO_5 + CaSO_4$	[76]
Structural	Porcelain	–	Porcelain	[77]
Structural	Si	–	$SiC + Si_3N_4 + SiON$	[78,79]
Structural	Si + SiC	(I) Silicone	SiSiC	[80]
Structural	SiC	(I) Si	SiSiC	[81,82]
Structural	Silicone	–	SiOC	[83]
Structural	Si_3N_4	–	Si_3N_4	[24]
Structural	SiO_2	(I) Al	$Al + Al_2O_3$	[84]
Structural	TiC	(I) Si	$Ti_3SiC_2 + TiSi_2 + TiC + SiC$	[85]
Structural	$TiC + TiO_2$	(I) Al	$Al + Al_2O_3 + TiAl_3$	[86]
Structural	$TiC + TiO_2$	(I) Al	$Al + Al_2O_3 + TiAl_3 + Ti_3AlC_2 + TiC$	[87]
Structural	$TiC + TiO_2$	(I) Al	$Al_2O_3 + TiAl_3 + Ti_3AlC_2$	[88]
Structural	TiO_2	(I) $[CH_3CH(O\text{-})CO_2NH_4]_2Ti(OH)_2$	TiO_2	[89]
Structural	Ti_3SiC_2	–	Ti_3SiC_2	[90,91]
Structural	WC + Co	–	WC + Co	[92–94]
Structural	ZrO_2	–	ZrO_2	[95]
Orthopedic	Bioactive glass	–	Bioactive glass	[96–98]
Orthopedic	Bioactive glass + $Ca_5(PO_4)_3(OH)$	–	Bioactive glass + $Ca_5(PO_4)_3(OH)$	[99]
Orthopedic	Bioactive glass + $Ca_3(PO_4)_2$	–	–	[100,101]
Orthopedic	Bioactive glass + $Ca_5(PO_4)_3(OH)$	–	$Ca_3(PO_4)_2 + Ca_5(PO_4)_3(OH) + Ca_2SiO_4$	[102]
Orthopedic	Bioactive glass + $CaCO_3$+silicone	–	$Ca_5(PO_4)_3F + Ca_5(PO_4)_3(OH) + CaSiO_3 + Ca_2SiO_4 + SiO_2$	[103]
Orthopedic	$Ca_8H_2(PO_4)_6{\cdot}5H_2O$	–	$Ca(HPO_4){\cdot}2H_2O + Ca_3(PO_4)_2$	[104]
Orthopedic	$Ca(HPO_4)$+$Ca(OH)_2$	–	$Ca(HPO_4) + Ca(OH)_2 + Ca_5(PO_4)_3(OH)$	[105]
Orthopedic	$Ca_2KNa(PO_4)_2$	–	–	[106]
Orthopedic	$CaO + Na_2O + P_2O_5$+SiO_2	–	$CaO + Na_2O + P_2O_5 + SiO_2$	[107,108]
Orthopedic	$[Ca(PO_3)_2]_n$	–	$[Ca(PO_3)_2]_n$	[109,110]
Orthopedic	$Ca_3(PO_4)_2$	–	–	[111–115]
Orthopedic	$Ca_3(PO_4)_2$	–	$Ca(HPO_4)$	[116–119]
Orthopedic	$Ca_3(PO_4)_2$	–	$Ca(HPO_4) + Ca(HPO_4){\cdot}2H_2O$	[120]
Orthopedic	$Ca_3(PO_4)_2$	–	$Ca(HPO_4) + Ca(HPO_4){\cdot}2H_2O + Ca_3(PO_4)_2$	[121–123]
Orthopedic	$Ca_3(PO_4)_2$	–	$Ca(HPO_4){\cdot}2H_2O$	[124]
Orthopedic	$Ca_3(PO_4)_2$	–	$Ca(HPO_4){\cdot}2H_2O + Ca_3(PO_4)_2$	[125,126]
Orthopedic	$Ca_3(PO_4)_2$	–	$Ca_3(PO_4)_2$	[115,127–137]
Orthopedic	$Ca_3(PO_4)_2$	(A) $MgO + SiO_2$	$Ca_3(PO_4)_2 + MgO + SiO_2$	[137]
Orthopedic	$Ca_3(PO_4)_2$	(A) MgO + SrO	$Ca_3(PO_4)_2$ + MgO + SrO	[135,136]
Orthopedic	$Ca_3(PO_4)_2$	(A) SiO_2 + ZnO	$Ca_3(PO_4)_2 + SiO_2$ + ZnO	[128]
Orthopedic	$Ca_3(PO_4)_2 + CaCO_3$	–	$Ca_3(PO_4)_2 + Ca_5(PO_4)_3(OH)$	[138]
Orthopedic	$Ca_3(PO_4)_2 + Ca_4(PO_4)_2O$	–	$Ca_4(PO_4)_2O + Ca_5(PO_4)_3(OH)$	[139]
Orthopedic	$Ca_3(PO_4)_2 + Ca_5(PO_4)_3(OH)$	–	$Ca(HPO_4) + Ca_3(PO_4)_2 + Ca_5(PO_4)_3(OH)$	[140]
Orthopedic	$Ca_3(PO_4)_2 + Ca_5(PO_4)_3(OH)$	–	–	[141,142]
Orthopedic	$Ca_3(PO_4)_2 + Ca_5(PO_4)_3(OH)$	–	$Ca_3(PO_4)_2 + Ca_5(PO_4)_3(OH)$	[143–146]
Orthopedic	$Ca_3(PO_4)_2 + Ca_5(PO_4)_3(OH)$ +$CaSO_4$	–	$Ca_5(PO_4)_3(OH) + CaSO_4{\cdot}2H_2O$	[147]
Orthopedic	$Ca_4(PO_4)_2O$	–	$Ca(HPO_4) + Ca(HPO_4){\cdot}2H_2O + Ca_3(PO_4)_2$	[123]
Orthopedic	$Ca_5(PO_4)_3(OH)$	–	–	[115,148–151]
Orthopedic	$Ca_5(PO_4)_3(OH)$	–	$Ca_5(PO_4)_3(OH)$	[35,115,129,152–157]
Orthopedic	$Ca_5(PO_4)_3(OH)$	(I) Bioactive polymer	Bioactive polymer + $Ca_5(PO_4)_3(OH)$	[158]
Orthopedic	$CaSO_4$	–	$CaSO_4{\cdot}0.5H_2O$	[159–161]
Orthopedic	$CaSO_4{\cdot}0.5H_2O$	–	$Ca_5(PO_4)_3(OH)$	[162]
Orthopedic	$CaSO_4{\cdot}0.5H_2O$	–	$CaSO_4{\cdot}2H_2O$	[163]
Orthopedic	$CaSO_4{\cdot}0.5H_2O$	–	$Ca_5(PO_4)_3(OH) + CaSO_4{\cdot}0.5H_2O$	[164]
Orthopedic	$CaSO_4{\cdot}0.5H_2O$	–	$Ca_5(PO_4)_3(OH) + CaSO_4{\cdot}2H_2O$	[162,163]
Orthopedic	$CaSO_4{\cdot}0.5H_2O$	–	$Ca(HPO_4) + Ca_5(PO_4)_3(OH) + CaSO_4{\cdot}2H_2O$	[163]
Orthopedic	$CaSO_4{\cdot}0.5H_2O$	–	$CaCO_3 + CaSO_4 + CaSO_4{\cdot}2H_2O$	[165]
Orthopedic	$CaSO_4{\cdot}0.5H_2O$	(A) $AgNO_3$	$Ag_3PO_4 + Ca_5(PO_4)_3(OH)$	[166]
Orthopedic	$CaSO_4{\cdot}0.5H_2O$	(I) $(C_6H_{10}O_2)_n$	$(C_6H_{10}O_2)n + Ca_5(PO_4)_3(OH)$	[162]
Orthopedic	$Mg_3(PO_4)_2$	–	$Mg_3(PO_4)_2$	[167]
Orthopedic	$Mg_3(PO_4)_2 + Mg_5Sr(PO_4)_4 + Mg_2Sr(PO_4)_2$	–	$MgHPO_4{\cdot}3H_2O + Mg(OH)_2 + SrCO_3$	[167]

Table 2 *Continued*

Application	Feedstock material	Additive (A) or infiltrant (I)	Resultant material	Reference
Orthopedic	$Mg_3(PO_4)_2 + (NH_4)_2HPO_4$	–	$NH_4MgPO_4{\cdot}6H_2O$	[168]
Electronic	Al_2O_3	–	Al_2O_3	[25,27,169]
Electronic	$BaTiO_3$	–	$BaTiO_3$	[27,170,171]
Electronic	Si_3N_4	–	Si_3N_4	[25]
Dental	Al_2O_3	(I) Dental glass	Al_2O_3 + dental glass	[172]
Dental	Dental porcelain	–	Dental porcelain	[173,174]
Dental	Dental porcelain	(A) Al_2O_3	Al_2O_3 + dental porcelain	[175]
Optical	SiO_2	–	SiO_2	[176]

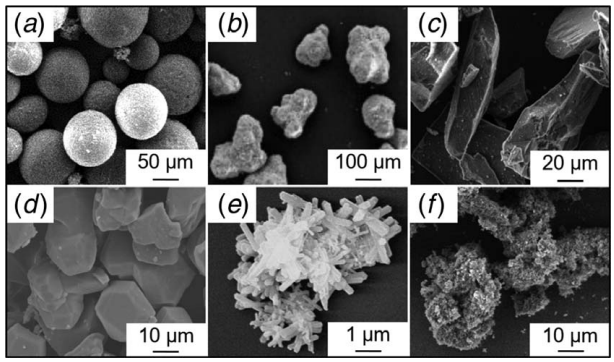

Fig. 4 Different ceramic particle shapes used in binder jetting: (*a*) spherical, (*b*) rounded [179], (*c*) angular, (*d*) polygonal [172], (*e*) irregular [102], and (*f*) aggregated

Coarse powder usually has good flowability, while fine powder often has good sinterability [111]. When the particle size is smaller than a certain value, the interparticle cohesion becomes more dominant than the inertia [188]. Therefore, fine particles tend to agglomerate, usually resulting in bimodal pore size distribution in the spread powder layer [147,165,189] and a low powder bed density. The particle size also plays a vital role in powder sinterability. The specific surface area of fine powder is larger than that of coarse powder, leading to a larger sintering driving force and consequently higher densification after sintering [98]. It is noted that larger particles are desirable for better flowability, while smaller particles are preferred for better sinterability. These two requirements on the particle size are contradictory.

Sun et al. reported that the poor flowability of a mixed glass-ceramic powder of relatively small particle size (<25 μm) caused powder adhesion onto the roller and thus the movement of the printed layer when spreading a new layer, eventually leading to a significant misalignment between printed layers [98]. In the study by Zocca et al. [97], lithium alumino-silicate glass powder with a median diameter of 75 μm (fine powder) had an *HR* value of 1.29 and the powder with a median diameter of 223 μm (coarse powder) had an *HR* value of 1.11, indicating the better flowability for the coarse powder.

2.3.5 Powder Deposition Methods. In binder jetting, the powder can be deposited with various methods. Figure 5 shows four powder deposition methods, where h is desired layer thickness and h_d is predeposited thickness. A parameter called the compaction ratio, which is the ratio of h_d to h, is used to quantify the compaction level, and a value of two is a common choice [75,170]. The effect of an amount increase of the predeposited powder, which induces a higher compaction ratio, has been experimentally studied [57]. It shows that green parts made with more predeposited powder have a higher bulk density.

Among all deposition methods, doctor blade spreading is the simplest, with little powder compaction occurring. Other three methods use a roller instead of a blade, and the roller can be fixed [151], forward-rotating [75], or counterrotating [151]. The counterrotating roller is the most commonly used. The traversing movement of the roller deposits compacts the powder, while the rotation smooths the powder bed. Compared with counterrotating roller, fixed roller and forward-rotating roller have not drawn much interest because of the higher surface roughness of the spread powder bed [151] and powder bed disturbance by the powder adhering onto the roller surface [75], respectively.

In a numerical study, a counterrotating roller outperforms the doctor blade in achieving high powder bed density and low surface roughness [190]. The combination of different methods, e.g., forward-rotating roller and doctor blade [75], has been reported to increase the powder bed density. Parameters of each deposition method can also be tuned to improve the powder bed density. For example, Shanjani and Ehsan [191] introduced an analytical model and calculated the powder bed density formed by a counter-rotating roller system. It was found that larger roller diameter leads to a denser powder bed. It should be noted that there is no research directly investigating the effect of different powder deposition methods on printed part properties.

Although submicron and nanometer powders can be easily sintered, it is not easy to spread them due to their high surface energy and thus agglomeration issue [192]. One possible method to address this problem is vibration-assisted spreading. For example, Sachs employed three different methods to vibrate different parts during the printing process, including the build platform, the powder bed surface, and the scraper [20], to spread ceramic powders with a particle size of about 20 μm. A vibrating counterrotating roller [192], although not used for ceramic materials, is

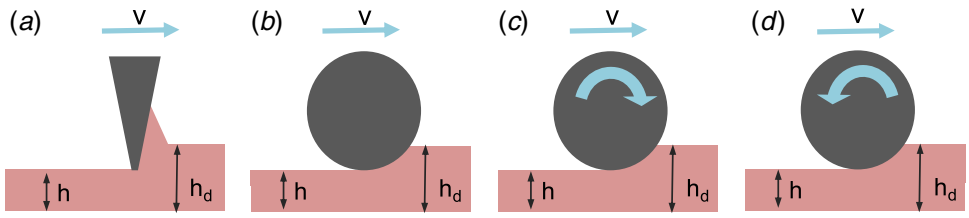

Fig. 5 Various powder deposition methods: (*a*) doctor blade, (*b*) fixed roller, (*c*) forward-rotating roller, and (*d*) counter-rotating roller. h is desired layer thickness and h_d is pre-deposited thickness.

Table 3 Binder materials in reported studies on ceramic binder jetting

Binder material	Reference
Carbohydrates (dextrin, maltodextrin, starch, etc.)	[37,54,68,71,80,82,85,86,88,96,99,102,107,108,115,144,145,148,149,155,156,158,162,163,166,167]
Phosphoric acid	[85,101,104,111–113,116,118–123,125,126,133,138,140,141,168]
Polymers (polyvinyl alcohol, polyethylene glycol, polyvinylpyrrolidone, etc.)	[23–25,27,37,57,58,64,65,67,69,73,80,94,95,109,110,114,134,142,143,153,157]
Colloidal silica	[6,7,18,20,72]
Acrylic acid	[23,27,79,146]

another potential method to break down agglomerates in fine powder with a particle size as small as 100 nm.

2.4 Binder

2.4.1 Binder Material and Concentration. Table 3 lists binder materials used in reported studies. Organic materials, including polymers (e.g., polyvinyl alcohol) and carbohydrates (e.g., dextrin), are the most common choice for the binder. They have the versatility to almost any powder and capability of thermal decomposition with little residue. Phosphoric acid is another common choice, especially for the scaffold parts from the calcium phosphate family. Colloidal silica is used in some cases where the binder is to be incorporated into the final component [18].

Binder concentration quantifies the amount of the adhesive material in the binder solution. For a powder–binder system in which chemical reaction happens between them, binder concentration could affect the green density. In the study by Gbureck et al. [120], tricalcium phosphate ($Ca_3(PO_4)_2$) part was printed with various phosphoric acid binder concentrations (5, 10, 20, and 30 wt%), and the green density was measured. Results show that the increase of binder concentration led to an improvement of the binder–powder reaction between tricalcium phosphate and the phosphoric acid forming dicalcium hydrogen phosphate ($CaHPO_4 \cdot 2H_2O$) and dicalcium pyrophosphate ($Ca_2P_2O_7$) as cement materials for the part [101,126,193]. They observed a downward trend of the green porosity. It should be noted that for a powder–binder system in which binder only bonds the particles together and does not involve any chemical reaction, binder concentration does not significantly affect the part density as the binder will be burnt off during debinding.

2.4.2 Binder Application Methods. Figure 6 illustrates two different methods of binder application. The first method, called binder jetting in-place, is to add the binder material to the printing solution and then jet the binder solution onto the powder bed [6,111,160,173]. The second is to pre-mix powder and binder by either a dry [109,110,163] or wet [85,142,158] approach and use the powder–binder mixture as the feedstock material. For dry mixing, the ceramic and binder materials are pre-mixed using a grinder, ball mill, or pestle and mortar. For wet mixing, the binder material is dissolved in a solvent (e.g., water), and the ceramic material is added to obtain mixture slurry. Then, the slurry is spray dried [35,68,100,101,115,127,129,138,142,146,148,149,152–155,158] or freeze dried [63,70,71,80,85,87,88] and sieved. For both dry and wet mixing, the binder within the powder feedstock joins the ceramic particles wherever the printing liquid (usually a water-based solution) is jetted.

Figure 7 shows the shares of each of the binder application methods in the reported studies. The binder jetting in-place method is less complicated than the other two due to fewer feedstock preparation steps and has the most shares in the reported studies. The powder–binder pre-mixing method allows for the use of a low-viscosity printing liquid because the binder is supplied in the powder feedstock, which decreases the possibility of nozzle clogging. Wet pre-mixing can be more advantageous than dry pre-mixing because the binder is more evenly mixed with the ceramic material.

2.5 Process Parameters

2.5.1 Layer Thickness. Layer thickness directly affects the time needed to print a part and the surface roughness of the part. Smaller layer thickness can lead to the smoother surface but a longer printing time, and vice versa [101]. The particle size is an important parameter to consider for selecting layer thickness. For binder jetting, there are no universally accepted rules for selecting layer thickness. Rules reported in the literature include at least greater than the largest particle size [75,165,194], twice the particle size [195], and at least three times the particle size [112,180].

Some studies have been reported about the effects of layer thickness on various material properties. Meier et al. employed a discrete element method model that considered particle-to-particle and particle-to-wall interactions involving frictional contact, rolling resistance, and adhesive forces [196]. It was found that the powder bed density increased with the increasing layer thickness. Some other studies found different effects of layer thickness on printed part density. For example, Shanjani and Ehsan introduced

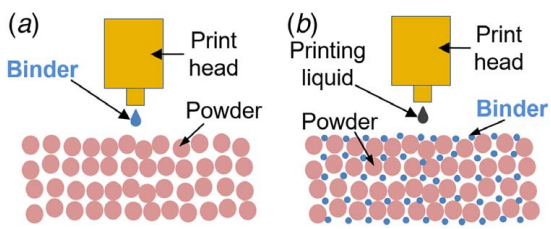

Fig. 6 Two binder application methods: (*a*) binder jetting in-place and (*b*) powder–binder pre-mixing

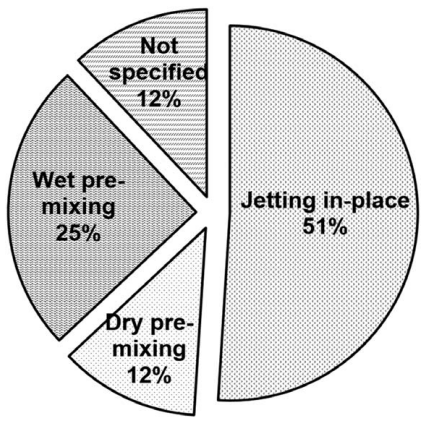

Fig. 7 Proportions of different binder application methods in the reported studies

an analytical model to predict the powder bed density under various layer thickness values [191]. The model was based on the mechanics of plastic strains of a volume-compressible continuum [197]. They found that an increase in layer thickness led to a decrease in the powder bed density.

2.5.2 Binder Saturation. Binder saturation, S_b, quantifies the amount of the binder solution applied during the printing process. It is defined as the percentage of air space (in the powder bed) that is filled with binder solution, given by the following equations:

$$S_b = \frac{V_b}{V_a} \tag{6}$$

$$V_a = (1 - \rho_p') \times V_e \tag{7}$$

where V_b is the volume of the binder applied to a predefined envelope, V_a is the air space volume of the powder bed within the same envelope before jetting binder, ρ_p' is the relative packing density of the powder bed, and V_e is the volume of the predefined envelope. It should be noted that the value of binder saturation may exceed 100% because the binder in the previous layers can dry out, and therefore, more binder than the presumed total free volume can be jetted to the powder [97].

A low binder saturation level leads to limited contact between the powder and the binder and results in fragile green parts. In contrast, a high binder saturation level causes the binder to spread out of the selected area, which is called bleeding, compromising the dimensional accuracy and surface smoothness of printed parts [179]. The effect of binder saturation on the sintered density was studied in the study by Sun et al.. A continuously decreasing trend of the sintered bulk density from 66.5% to 55.9% on titanium silicon carbide was reported with the increase in the saturation level of a commercial binder from 10% to 30% [90], which may be due to the increased surface roughness resulted from binder bleeding and thus larger apparent porosity. Melcher et al. found that the bulk density of sintered alumina parts from granulated powder (granule size of <150 μm) increased from 56% to 67% with the increase of the binder saturation of a water-based commercial binder from 0.14 g/cm^3 to 0.35 g/cm^3 [63]. It might be due to stronger particle bonding and thus denser green part after printing with the higher binder saturation.

3 Terminologies, Measurement Methods, and Achieved Values for Density and Porosity

3.1 Definition of Various Terminologies. Density and porosity are the most commonly assessed material properties in ceramic binder jetting. There are many terminologies related to density and porosity, dependent on what packing state the powder is in, what processing stage the part has gone through, and what pores are included in the calculation. The definitions are not always made clear in the published reports. These terminologies and their definitions are summarized in Table 4.

3.1.1 Powder Density in Different Packing States. There are three terminologies to define the powder density depending on different packing states: apparent density, tap density, and powder bed density. Apparent density is the density of freely settled powder [199–202]. Tap density is the density of a powder that has been tapped, to settle contents, in a container under specified conditions [181,182]. Powder bed density is the density of the powder that is spread on the build platform. Unlike the apparent density and the tap density that can be measured by following standards [181,182,199–202], the powder bed density can be measured by various methods. A common method is to spread a number (e.g., 50) of layers of powder and then measure the bulk volume and the mass of the powder [63,75,170]. Another method is to print multiple cylindrical cups and then measure the cup size and weight change after depowdering [203]. For a given powder, powder bed density is usually between those of apparent and tap densities.

3.1.2 Part Density After Different Process Stages. Green density, brown density, and sintered density are the part densities that just after printing, debinding, and sintering, respectively. Green and sintered densities have been vastly investigated, while brown density has been rarely reported for the friability of the debound part and thus the difficulty of density measurement. Other densities can be obtained if additional postprocessing steps are applied. For example, the infiltrated density can be measured if infiltration is performed [69,82,85,88,158,162] and the pressed density can be obtained if isostatic pressing is implemented [64,91,94].

Relative density (ρ') is the ratio of the absolute density (ρ) to the theoretical density (ρ_{th}):

$$\rho' = \frac{\rho}{\rho_{th}} \tag{8}$$

Table 4 Terminologies for density and porosity

Category	Terminology	Definition	Reference
Powder density in different packing states	Apparent density	Density of freely settled powder	[97,98,111,147]
	Tap density	Density of powder after standard tapping process	[97,98,147,155]
	Powder bed (packing) density	Density of powder that is spread on the build platform	[23–25,63,80,94,99,147,172,174]
Part density after different process stages	Green density	Density after printing	[23,25,80,88,99,110,120,143,155]
	Brown density	Density after debinding	[198]
	Sintered density	Density after sintering	[63,70,71,78,85,87,92,96,97,102,103,108,135–138,144,146,174]
Part density and porosity when different pores are included	Apparent solid density	Mass per unit apparent solid volume (total volume of solid material and closed pores)	[68,149,169,170]
	Bulk density	Mass per unit bulk volume (total volume of the solid material, open pores, and closed pores)	[98,130,135,136,158,162]
	Apparent porosity	Volume percentage of open pores in the bulk material	[63,84,97,98,105,110,120,124,125,134,143,149,155,157,161,164,167,175]
	Closed porosity	Volume percentage of closed pores in the bulk material	[128,130,135,136]
	Bulk porosity	The sum of apparent and closed porosity	[83,87,96,100,103,117–119,127,144,160]

where the theoretical density (ρ_{th}) is calculated based on the crystal structure and unit cell dimensions. In this paper, relative densities are used since they can be readily compared across various materials.

3.1.3 Part Density and Porosity Including Different Pores. For a part with both open and closed pores, its volume measurement is complicated. Figure 8 schematically shows these pores in a part. Open pores are permeable from a surface, while closed pores are not. The bulk volume of the part includes volumes of solid as well as both open and closed pores, while the apparent solid volume includes volumes of solid as well as closed pores. The only difference between these two volumes is that the bulk volume includes open pores but the apparent solid volume does not. Accordingly, the bulk density is the mass per unit bulk volume, while the apparent solid density is the mass per unit apparent solid volume. Similarly, apparent porosity [204], closed porosity, and bulk porosity are the fractions of the volumes of open pores, closed pores, and both of them, respectively, in the bulk volume. The bulk porosity (π_b), apparent porosity (π_a), and closed porosity (π_c) can be estimated from the relative apparent solid density (ρ'_{as}) and relative bulk density (ρ'_b) based on the following equations:

$$\pi_b = 1 - \rho'_b \tag{9}$$

$$\pi_a = 1 - \frac{\rho'_b}{\rho'_{as}} \tag{10}$$

$$\pi_c = \frac{\rho'_b(1 - \rho'_{as})}{\rho'_{as}} \tag{11}$$

The methods for the part density and porosity measurement are listed in Table 5. The geometry method works for a part with a simple shape (e.g., cuboid and cylinder). The simple Archimedes' method measures two kinds of sample masses: dry mass and immersed mass in water (to calculate the immersed volume). Usually, water is infiltrated into the open pores. The immersed volume is the apparent solid volume. Therefore, the simple Archimedes' method only measures the apparent solid density. Compared with that, full water absorption into the open pores is induced in the modified Archimedes' method by boiling [204,205] or vacuuming [204,206,207], after which immersed mass and soaked mass (in addition to dry mass) are measured to evaluate the open pore volume [204]. Therefore, this method is capable to simultaneously measure apparent solid and bulk densities.

In the mercury intrusion method, mercury is used as a nonwetting liquid is and does not enter open pores unless under pressure. The volume of the pores is determined from the mercury volume intruded at each pressure increment [208]. Gas pycnometer has a similar principle with that of simple Archimedes' method but with a displacement medium of gas (e.g., helium), which is suitable for physically or chemically sensitive materials [209] or for small pores. Computed tomography is a nondestructive method, which uses an X-ray and a mathematical algorithm to generate cross-sectional images of the part [210]. From these cross-sectional images, the volume can be determined. The image analysis method uses 2D images of the sample cross section and quantifies the porosity [170].

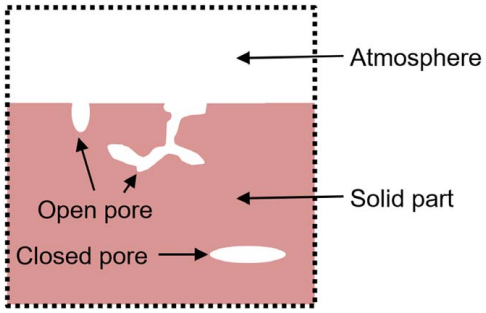

Fig. 8 Open and closed pores in a cross section of a part

3.2 Achieved Part Density in Reported Studies. As relative densities and porosities can be readily compared across different materials, all absolute values have been transformed to relative values based on Eq. (8). Theoretical density values are shown in Table 6. It should be noted that only materials whose density values were reported in absolute values are shown in this table.

Figures 9 and 10 show the achieved relative densities and porosities of the green and sintered parts. Different densities and porosities are interpreted by the reported terminologies and measurement methods in the corresponding papers. Special treatment techniques are used to categorize all values. Specific data values of Figs. 9 and 10 and the corresponding references are shown in Appendices A and B, respectively. It should be noted that besides these 83 density and porosity values from 65 publications, there are some unclear values because of the lack of specific description of the measurement method or nonstandard metrics (e.g., porosity derived from apparent solid density).

Green bulk density determines the sintered bulk density and thus other material properties. A slurry feedstock usually leads to a green bulk density of higher than 50%. Using a slurry with a 35 vol% alumina (0.5 μm), a green bulk density of 67% was achieved in the study by Grau et al. [24], which is the highest in the literature. Mixing powders of different sizes is another commonly used method to improve green density. Kunchala and Kappagantula [58] introduced alumina nanoparticles (less than 50 nm) to the binder and the printed alumina powder feedstock with an average size of 40 μm. A green bulk density of 65.7% was obtained when the nanoparticle concentration in the binder was 15 wt%.

Table 5 Capabilities of different density and porosity measurement methods

Method	Bulk density	Apparent solid density	Bulk porosity	Apparent porosity	Closed porosity	Reference
Geometry	Yes	No	Yes	No	No	[95,113,130,135,136,139,146,158,162]
Simple Archimedes'	No	Yes	No	No	No	[68,95,98,168–170]
Modified Archimedes'	Yes	Yes	Yes	Yes	Yes	[37,69,83,86–88,96,97,102,103,109,110,128,132,148,149,155,157,171]
Mercury intrusion	Yes	Yes	Yes	Yes	Yes	[23,63,70,71,108,143,156,163]
Gas pycnometer	No	Yes	No	No	No	[82,105,139,146]
Computed tomography	Yes	Yes	Yes	Yes	Yes	[141,144,160,161]
Image analysis	Yes	Yes	Yes	Yes	Yes	[170]

Table 6 Theoretical density values of different materials

Material	Theoretical density (g/cm^3)	Reference
Al_2O_3	3.97	[211]
AlN	3.25	[211]
$BaTiO_3$	6.02	[211]
$CaSO_4$	2.32	[212]
SiC	3.22	[211]
TiC	4.91	[211]
$TiAl_3$	3.40	[213]

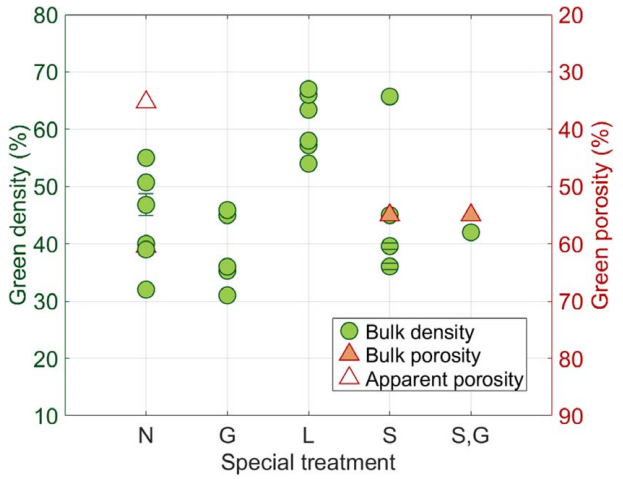

Fig. 9 Achieved values of relative green densities and porosities by various special treatment techniques (N stands for no special treatment, G for powder granulation, L for using slurry feedstock, and S for mixing powders of different sizes) [23–25,27,37,54,55,57,58,63,64,67,68,73,74,81,82,86–89,92,110,156,161]

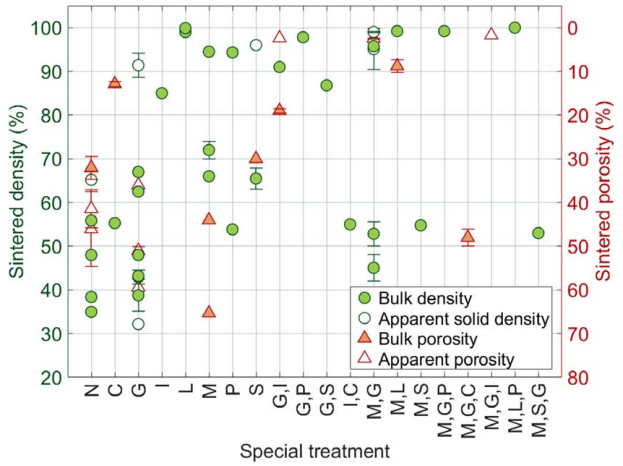

Fig. 10 Achieved values of relative sintered densities and porosities by various special treatment techniques (N stands for no special treatment, C for chemical reaction, G for powder granulation, I for infiltration, L for using slurry feedstock, M for mixing different materials, P for pressing, and S for mixing powders of different sizes) [24,27,37,53,55,63–65,68–71,77,83,85,86,88–90,92,94–98,100,102,103,108–110,127,128,130,132,135,136,144,146,149,155–158,169,170,174]

Sintered bulk density directly determines other material properties. Therefore, it is mostly reported in the literature. A high sintered bulk density (>90%) was achieved in some studies by applying slurry feedstock [24,27,37,94], infiltration [86], or isostatic pressing [64,90,94]. The slurry feedstock is among the most effective techniques. In the study by Cima et al. [27], parts printed with alumina slurry achieved a green bulk density of 58% and a sintered bulk density of 99.9%. Combinations of special treatments can lead to high sintered bulk density as well. Specifically, Kernan et al. [94] studied the printing of tungsten carbide with an average particle size of 0.8 μm, in which a combination of mixing different materials (tungsten carbide and cobalt), slurry feedstock (25 vol. % water-based slurry), and hot isostatic pressing (HIP; 5.5 MPa during sintering) was applied, and the achieved sintered bulk density was 100%. A bulk density of 99.2% was achieved by using an alumina slurry feedstock (0.5 μm, 34 vol%) in combination with applying sintering additives in the study by Zocca et al. [37]. Bulk density of the printed alumina part increased from 34% to 61% by warm isostatic pressing (WIP) in the study by Yoo et al. [64], leading to a sintered bulk density of 99.2% (with the additional help of sintering additive and powder granulation).

4 Material Preparation Techniques for Density Improvement

4.1 Powder Granulation. The contradiction between the flowability and the sinterability of the feedstock powder is among the main challenges in the field of ceramic binder jetting. Generally, the particle size used in binder jetting is in the range of 10–100 μm to ensure a good flowability and avoid defects in powder bed layers. At the same time, the particle size should be less than 1 μm to ensure a high sinterability and thus a dense part after sintering [64]. However, the flowability of fine powder (less than 1 μm) is usually not high enough to form a uniform and smooth layer of powder bed due to its high interparticle cohesion [151,214]. Fine powder spreading usually creates pores and cracks on powder bed, which are consequently inherited by the green and sintered parts. Therefore, increasing the flowability of fine powder is highly beneficial to fabricate dense parts with a minimal number of pores.

One common technique to increase the powder flowability is granulation [215,216]. The granulated powder can significantly improve the flowability of the feedstock powder. The fine raw particles ensure the required sinterability, and the coarse resultant granules ensure the required flowability. Its principle is schematized in Fig. 11. Basically, raw (fine) particles are bonded by a binder to form larger aggregates (or granules). Steps for granulation include mixing, drying, comminuting, and sieving, as shown in Fig. 12 and listed in Table 7. A ball mill, grinder, or pestle and mortar can be used to mix raw particles with a binder solution to form a slurry, which can be dried by a spray dryer, freeze dryer, or oven. The comminuting step is not needed for the powder from a spray dryer because the size is determined by sprayed droplets. For the cakes dried by a freeze dryer or an oven, comminuting step is needed to decrease the size by ball milling, grinding, or manual crushing. Then, a sieving step screens the powder into several groups with different size ranges. Generally, the manual granulation method, comprising manual mixing in a crucible, oven drying,

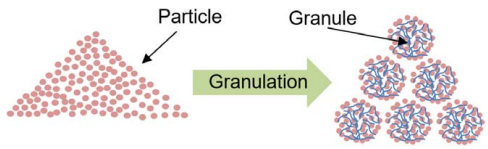

Fig. 11 Principle of granulation

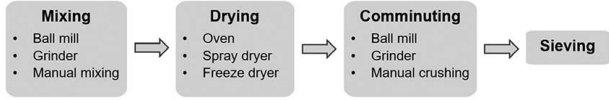

Fig. 12 Basic granulation steps

Table 7 Granulation processes practiced in reported studies

Granulation process	Reference
Dry mixed, dry ball milled	[86]
Dry mixed, sieved	[80]
Wet mixed, (wet ball milled), spray dried	[68,100,101,127,128,142,146,148,149,153,155,158]
Wet mixed, (wet ball milled), oven dried, dry ball milled	[78,130,135–137]
Wet mixed, (wet ball milled), freeze dried, dry ball milled, sieved	[63,70,71,85,87,88,95]
Commercial spray-dried powder	[35,129,152,154]

Table 8 Reported studies on mixing powders of different sizes

Material	Size (μm)	Mixing ratio	Reference
Al_2O_3	2, 10, 70	17.6:21.1:61.3	[65]
Al_2O_3	30, 45, 53	1:1:1	[169]
Al_2O_3	20, 3.4, 0.4	63:27:10	[67]
Al_2O_3 and Al	0.6, 3	25:100, 30:100, 35:100, 40:100, 50:100	[54]
$Ca_3(PO_4)_2$ and bio-glass	8, 38	1:3, 1:1	[100]
$Ca_5(PO_4)_3(OH)$	38, 125	15:85, 25:75, 35:65	[148]
$Ca_5(PO_4)_3(OH)$	4, 50	15:85, 25:75, 40:60, 60:40, 75:25, 100:0	[156]
Glass-ceramic compound	0–25, 45–100	0:100, 10:90, 20:80, 30:70, 40:60, 100:0	[98]

manual crushing in a crucible, and finally sieving, is simple, although the granule shape is irregular. Commercial granulation machines based on spray drying technologies, although costly, can produce spherical and large-batch granulated powder.

Chumnanklang et al. [149] investigated the effect of binder fraction on the flowability of spray-dried hydroxyapatite powder. The powder flow rate increased from 14.6 to 21.2 g/s when the binder fraction decreased from 48.3 to 15.7 vol%. Gildenhaar et al. prepared spray-dried calcium alkaline phosphate powder with various raw particle sizes [106]. They found that printed parts made with granules from fine raw powder (3.1 μm) had a higher compressive strength (2.5 MPa) than those from coarse raw powder (7.5 μm, 1.80 MPa).

With the same raw powder, different granulation technologies can result in different material properties. Suwanprateeb et al. [155] studied two granulation technologies, manual granulation with mortar and pestle and spray drying. After printing and sintering at 1300 °C, samples made with manually granulated hydroxyapatite powder showed ~20% higher bulk density and approximately two times higher flexural modulus and strength than those made from spray-dried powder. One of the reasons is the larger number of intergranule pores from the spray-dried powder than the manually granulated powder, leading to a lower green density. Another possible reason is the large pores within the spray-dried granules, which are formed due to the solvent evaporation during the drying process [217].

These two issues of spray-dried granules can be potentially resolved by another granulation technique called spray freeze drying [218–220]. The granules from spray freeze drying can be soft, making the particles loosely bonded and easily breakable. The granules can be crushed by externally exerted forces such as the roller compaction force. Therefore, the granules retain a microscale size before spreading and facture to a nanoscale size after compaction. The other feature of the granules from spray freeze drying is its homogeneous structure. No large pores are formed inside a granule after drying as the sprayed droplet is frozen first and the drying process is solvent sublimation instead of evaporation [218].

4.2 Mixing Powders of Different Sizes. Particle size distribution plays a key role in powder packing, which can be either monomodal or multimodal. Since fine particles can fill voids between coarse particles, powder with a multimodal size distribution has less interparticle voids. From this point of view, mixing powders of different sizes can be an effective technique to increase the powder bed density and consequently green density of printed parts [65]. Moreover, this technique could also reduce sintered shrinkage as there are less voids in the green part. This is beneficial for improving the dimensional accuracy after sintering.

Table 8 lists studies on mixing powders of different sizes for feedstock preparation. For example, Sun et al. studied the effects of powder mixing on powder flowability, part sintered density, and part bending strength [98]. Glass-ceramic powders with three size ranges were mixed in various fractions. The mixture with 60 wt% 45–100 μm and 40 wt% 0–25 μm particles achieved the highest sintered bulk density of 1.6 g/cm^3 and bending strength of 13.8 MPa. In Spath et al.'s experiment, parts made from mixed hydroxyapatite powder had a higher compressive strength than those from the two constituent powders [148].

Instead of finding the optimal ratio by trial and error, a promising direction is model-guided selection of particle size and mixing ratio of constituent powders. In the study by Du et al. [65], packing densities with various mixing ratios were predicted using the linear packing model [221]. Optimal mixing ratios to achieve the highest packing density were selected for both binary and ternary mixtures. The printed parts from optimal ternary ratios achieved the largest sintered bulk density. Although the improvement is small due to the decreased flowability, the study showed that the linear packing model has a potential to guide the selection of the particle size and mixing ratio.

Another method to mix powders of different sizes is to introduce nanoparticles of the same material during printing [58,95]. These nanoparticles can enhance the sintering performance due to their high activity. For example, Zhao et al. demonstrated the feasibility of using 10 wt% zirconia nanoparticle suspension as the printing liquid while printing zirconia parts [95]. The printed and sintered bulk density increased from 75.2% to 86.8% as the binder saturation increased from 50% to 120%.

4.3 Slurry Feedstock. Structural ceramic parts usually require fine-grained powder (submicron) and high green density (>50%) to achieve a full density after sintering [24]. However, it is difficult to meet these requirements simultaneously using dry powder feedstock. Due to its low packing density and agglomeration issues, dry fine powder feedstock generally results in parts with low green density and defects.

The slurry feedstock was used to meet both requirements of fine powder and high green density [24–31,37,77,81,94]. In this technique, a layer of ceramic slurry is deposited and then dried to form the powder bed [26]. Two slurry deposition methods have been reported in the literature. The first one is nozzle jetting [23–25,27,94,176] that was studied by the inventors of binder jetting. In this case, a thin slurry layer is deposited by a single nozzle scanning over a porous substrate [25]. The second deposition method is doctor blade spreading that was studied by Zocca et al. [37,81] and Lima et al. [77]. In both deposition methods, the layer top is dried by a heating lamp, while the bottom was dried due to capillary forces from the porous substrate or previously deposited and dried layers [24,222]. Delicate temperature and ventilation control are needed to achieve crack-free powder bed layers.

Compared with the dry powder deposition method, the slurry-based method can handle the submicron particle size (down to 0.5 μm). It can achieve high powder bed density (up to 53% in the study by Kernan et al. [94]) and high green part bulk density (up to 67% in the study by Grau et al. [24]). Different materials (i.e., alumina [24,25,27,37,77], silicon nitride [24,25], silicon

carbide [81], silica [176], and tungsten carbide with cobalt [94]) have been investigated with this method. In the study by Zocca et al. [44], printed parts from an alumina slurry (solid loading of 34 vol% and average particle size of 0.5 μm) achieved near theoretical density (i.e., bulk density of 99.2%) after sintering on 1600 °C with the help of sintering additives.

Maximum layer thickness, i.e., critical saturation thickness (CST) [30], exists for the slurry feedstock technique. A layer thickness larger than the CST leads to cracking or warping of the powder bed due to the capillary pressure of solvent evaporation [24,26,30]. Furthermore, thick parts are prone to crack and difficult to be fully dried [49].

It should be noted that the slurry feedstock has been extensively used in other ceramic AM technologies such as vat photopolymerization and material extrusion. For example, Hu et al. prepared a 60 vol% alumina slurry (average size of 138 nm) [223] for vat photopolymerization. After printing and sintering at 1650 °C for 2 h, the part achieved a bulk density of 3.96 g/cm^3 (99.7% in relative). Mamatha et al. [224] used slurry with a solid loading of 64.75 wt% of alumina powder (average size of 331 nm) in material extrusion. After printing and sintering at 1650 °C for 1 h, the part achieved a bulk density of 97.7%. Therefore, the application of slurry feedstock in binder jetting can be advanced by learning from other AM technologies.

4.4 Mixing Different Materials. Mixing different materials is a common technique to increase printed and sintered density [77,92,96–98,100,102,105,108,120,123,124,128,138,139,141,143,144, 146,174]. The mechanisms for density enhancement could be boosting the mass transport [37,74,128,135–137] or enabling liquid-phase sintering [225]. Yoo et al. doped alumina (mean particle size of 0.8 μm) with MgO and granulated both undoped and doped powders to a granule size ranging from 70–150 μm [64]. The printed and sintered parts from doped alumina achieved a higher relative sintered bulk density (99.2%) and flexural strength (324 MPa) than the undoped powder (97.8% and 231.6 MPa) after printing, isostatic pressing, and sintering.

Although this mixing technique could be effective, other material properties (e.g., biocompatibility) may be impaired. The limited choice of additive materials is one of the drawbacks of this technique. Moreover, the additive particles may not be homogenously distributed within the ceramic powder, leading to structure heterogeneity (i.e., local variation) in the sintered part [52,226]. In addition, the selection of additives has remained largely empirical as the mechanism of the sintering additive has not been fully understood [226]. Therefore, this technique only works for specific materials.

5 Postprocessing Techniques for Density Improvement

5.1 Sintering. Sintering is the process by which a powder compact is transformed to a dense body by heating [227]. It is the most commonly used method to increase the density. Sometimes it is considered an essential part of the process and not considered a separate postprocessing method. The macroscopic driving force in sintering is the reduction in surface energy. The densification during sintering happens by the elimination of solid/vapor interfaces [227]. However, sintering is not required in some cases, for example, when porous parts are preferred or other postprocessing techniques are applied.

One of the important sintering parameters is the sintering temperature. Sintering temperature significantly affects the material properties as it determines the mass transport of the ceramic particles. Typically, a higher sintering temperature can facilitate mass transport and subsequently increase the part density and the decrease porosity [53]. Another parameter significantly that affects the sintered density is the green density. To present the effect of the green density on the sintered density, the bulk densities before and after sintering are shown in Fig. 13. The powder bed density

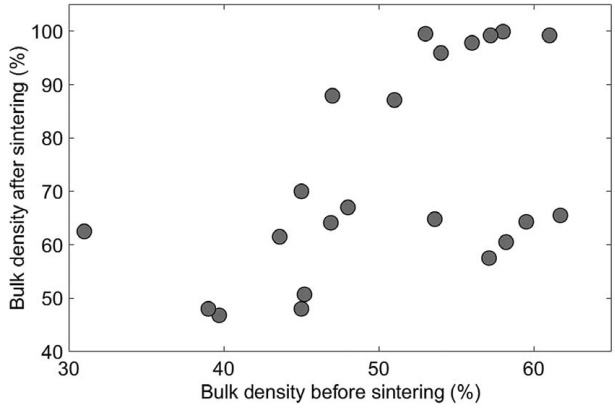

Fig. 13 Bulk densities before and after sintering [24,27,37,55,63–65,68,83,89,94,156]

is also included as it is close to green density. As some parts were isostatically pressed before sintering [64], their pressed green densities are presented instead of printed green densities. Specific data values of Fig. 13 and the corresponding references are shown in Appendix C. Generally, high green density leads to high sintered density. A high green density (i.e., >50%) is required to achieve a high sintered density (i.e., >90%).

Shrinkage is a critical index to determine the density change by sintering. For parts with the same green density, a larger shrinkage leads to a higher sintered density. A primary factor that affects shrinkage is sinterability, which is directly related to particle size [228]. For example, Du et al. [65] used alumina powder with an average particle size of 10 μm and achieved a powder bed density of 57.1%. By using 0.5 μm alumina powder, Zocca et al. [37] achieved a green density of 57.2%. As there is no significant density change for the powder bed after printing, it can be assumed that green parts from Du et al.'s and Zocca et al.'s studies have approximately the same green densities. After sintering at 1600 °C, parts made from coarse powder (10 μm alumina in the study by Du et al.) achieved only 0.7% volumetric shrinkage, leading to a bulk density of 57.7%. However, parts from fine alumina powder (0.5 μm in the study by Zocca et al.) achieved a volumetric shrinkage of 73.4% and the bulk density of 99.2%.

It should be noted that sintering could also result in shape distortion due to gravity effect, nonuniform temperature gradient, liquid-phase formation due to high sintering temperature, etc. [229]. For example, Grant et al. [89] studied the distortion of printed titanium dioxide cantilever beams at different sintering temperatures up to 1420 °C. It was found that most of the distortion happened above 1180 °C. To mitigate the distortion, they infiltrated the printed parts with an aqueous precursor solution and then heated the parts at 300 °C to decompose the precursor to form titanium dioxide nanoparticles through hydrothermal reactions. The distortion of infiltrated beams (1 mm) was 75% less than that of uninfiltrated beams (4 mm) after sintering at 1420 °C for 10 h.

5.2 Chemical Reaction. Chemical reaction is another common method to increase green and sintered densities in ceramic binder jetting, which includes metal oxidation [53,54,79,84], phosphoric acid immersion for calcium phosphate materials [113,117,119,120,122,123,125,126,141,162,163], and pyrolysis of preceramic polymers [83,103]. Metal oxidation uses metal powder as the feedstock material and converts a printed metal part to a ceramic one by oxidation at a high temperature. Phosphoric acid immersion uses this acid solution to immerse calcium phosphate parts, which are printed with a binder of phosphoric acid solution. The immersion leads to a further reaction of unreacted material and thus a cemented structure. Pyrolysis of preceramic polymer uses polymeric precursor as the feedstock and ceramize the printed part at a high temperature.

For example, Zocca et al. [83] investigated the possibility of using silicone (polymethylsilsesquioxane) as a preceramic polymer. A bulk density of 87.1% for the ceramized SiOC part was achieved after sintering at 1200 °C for 1 h. It should be noted that the chemical reaction technique works only for certain material systems. Specifically, the ceramization reaction in the preceramic polymer pyrolysis technique involves a significant mass transport of the reagents and/or the by-products. Therefore, the part size is limited with this technique.

5.3 Infiltration. Infiltration is another common method to increase the part density. Both a different material [71,85,88,89,162] and the same material [69] have been investigated to infiltrate parts from binder jetting. The most common infiltration method is melt infiltration [44,63,70,71,80,82,85–88,162,172]. In the study of Nan et al. [85], the printed and sintered TiC parts were infiltrated in melted silicon at 1600–1700 °C for 1 h and annealed at 1400 °C for 2 h, which produced Ti_3SiC_2 (about 45 vol%), $TiSi_2$ (about 21 vol%), and SiC. Infiltration with different materials changes the composition of a part, and the resultant phases might be difficult to control sometimes.

Solution infiltration can be used for infiltrating a part with the same material, in which fine powder is mixed with a solvent and the part is immersed in it. The most critical parameter for this infiltration method is solid loading. For example, Maleksaeedi et al. [69] printed and pre-sintered alumina parts at 1000 °C for 2 h, infiltrated them in alumina slurries of different solid loadings, and post-sintered them at 1650 °C for 2 h. As the solid loading increased from 0 (no infiltration) to 50%, the bulk density of the final parts increased from 38% to 85%. Cross sections of the infiltrated parts after post-sintering are schematically shown in Fig. 14. The infiltration depth for parts with the same shape and size decreased along with the increase of solid loading. A noninfiltrated core remained in the parts treated with slurry of a high solid loading.

Another method is precursor solution infiltration followed by hydrothermal reactions of the precursor to generate the ceramic material. For example, Grant et al. printed parts with titanium dioxide powder with a particle size of <63 μm [89]. Then, the printed parts were infiltrated by a 50 wt% aqueous solution of titanium (IV) bis(ammonium lactato) dihydroxide, followed by heating the parts at 300 °C to turn the precursor into titanium dioxide. The infiltrated parts achieved a density of 55% after sintering at 1420 for 10 h, compared with 48% of uninfiltrated parts. Moreover, the distortion of infiltrated parts (1 mm) was 75% less than that of uninfiltrated parts (4 mm) after sintering.

5.4 Isostatic Pressing. Isostatic pressing is a traditional powder metallurgy process that applies equal pressure in all directions on a powder compact, thus achieving uniform density and microstructure [211,230], The pressing medium that exerts equal pressure can be water, oil, and gas. Based on the operation temperature, this technique is classified as cold isostatic pressing (CIP), WIP, and HIP [230,231]. CIP can consolidate green parts under room temperature to obtain higher green density ready for sintering. WIP operates at intermediate temperatures from 80 °C to 450 °C [231], which is suitable for parts requiring a heat-induced chemical reaction [230]. HIP heats and presses the part under gas medium (e.g., argon) with accurate control of both temperature (up to 2000 °C) and pressure (50–200 MPa) [230]. It usually requires longer processing time than CIP and WIP.

All three kinds of isostatic pressing techniques have been utilized in ceramic binder jetting. For example, Sun et al. used CIP method to consolidate green Ti_3SiC_2 bodies [90], which led to an increased sintered bulk density of 94.3% compared with 65.5% without CIP. In the study by Yoo et al., both CIP and WIP were utilized to densify alumina green parts. The bulk density increased from 36% to 54% after CIP and 34% to 61% after WIP, which resulted in sintered bulk densities of 95.9% and 99.2%, respectively [64]. Printed AlN parts were heated to 2000 °C and pressed at 310 MPa for 8 h by HIP, leading to a bulk density of 60.1% [55]. Isostatic pressing can increase green and thus sintered densities significantly, but it is not applicable to parts of complex geometries such as internal cavities.

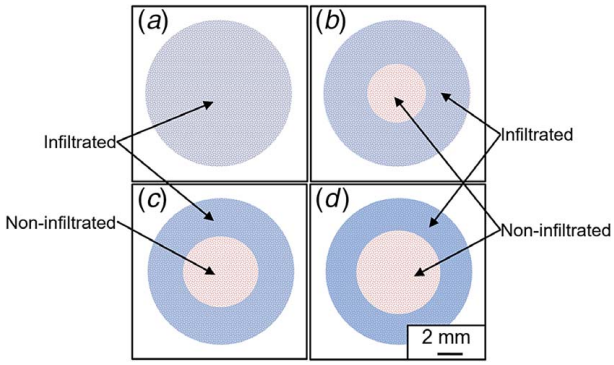

Fig. 14 Schematic illustration of cross sections of parts infiltrated at various solid loadings: (*a*) 35%, (*b*) 40%, (*c*) 45%, and (*d*) 50% [69]

6 Knowledge Gaps

To produce dense ceramic parts by binder jetting followed by pressureless sintering, fine powder (e.g., less than 1 μm) is needed because it has a large specific surface energy and thus allows for a high densification level through sintering [52]. However, the spreading, compaction, and densification behaviors are still not well understood.

6.1 Spreading Behavior. The fine powder is known for its spreading difficulty: it is challenging to form a dense, smooth, and uniform powder bed. It is generally accepted that the spreading difficulty is a result of interparticle cohesion. However, the nature of the interparticle cohesion is not clear. When discussing the interparticle cohesion, researchers usually refer to van der Waals interaction and electrostatic interaction. Hydrogen bonding and capillary bridging are often overlooked. They could play an important role in powder spreading. In addition, the spreader design, spreading strategy and parameters, and environmental humidity can also affect the spreading behavior. However, these effects are still not well understood.

6.2 Compaction Behavior. A high powder bed density is needed to have high green and consequently sintered densities. An effective way to increase powder bed density is compaction, during which the externally applied stress exceeds the yield strength of the powder and leads to particle rearrangement [232,233]. Several compaction approaches, including a forward-rotating roller [64,234] and compaction plate [78], have been reported. However, important issues about this layer-by-layer compaction have not been studied. For example, effects of compaction parameters on the powder bed and its uniformity within the same layer or across different layers are critical but unknown.

6.3 Densification Behavior. The densification behavior of fine powder has been studied for traditional ceramic pressing and sintering. However, binder jetting poses unique challenges for densification. For example, the green density from binder jetting is usually not as high as that from pressing. It is necessary to understand the densification behavior of loosed packed particles. In addition, binder jetting is developed for producing parts with complex geometries. The relationship between geometry and densification is not well understood.

7 Concluding Remarks

Ceramic binder jetting additive manufacturing has many advantages. The main limitation preventing its widespread industrial applications seems to be related to the low density (and thus inferior mechanical properties) of printed parts. While various density terminologies have been used for parts by binder jetting, bulk density is more suitable in technical communications for structural applications as it directly determines mechanical properties. It has been reported that special treatment techniques could improve the bulk density. However, most of these techniques have drawbacks, making them inappropriate for a wide range of applications. Granulation is a promising technology, but the literature does not contain sufficient studies on how to eliminate intragranule and intergranule pores. The fine powder is needed to obtain dense ceramic parts by binder jetting, but there are no sufficient studies on its spreading, compaction, and densification behaviors.

Acknowledgment

This material is based upon work supported by the National Science Foundation (Grant No. 1762341).

Appendix A: Supplementary Data for Fig. 9

Special treatment	Density or porosity type	Value (%)	Standard deviation (%)	Reference
–	Bulk density	32	–	[55]
–	Bulk density	39	–	[89]
–	Bulk porosity	60.5	1.4	[110]
–	Bulk density	40	–	[82]
–	Bulk density	46.8	1.9	[57]
–	Bulk density	50.7	–	[58]
–	Bulk density	55	–	[73]
–	Apparent porosity	35.28	–	[161]
G	Bulk density	31	–	[64]
G	Bulk density	35.3	–	[63]
G	Bulk density	36	–	[64]
G	Bulk density	42	–	[92]
G	Apparent solid density	45	–	[68]
G	Bulk density	45.9	–	[86]
L	Bulk density	54	–	[25]
L	Bulk density	57.2	–	[37]
L	Bulk density	58	–	[27]
L	Bulk density	63.4	–	[23]
L	Bulk density	66	–	[77]
L	Bulk density	67	–	[24]
S	Bulk density	36.05	0.57	[54]
S	Bulk density	39.6	0.6	[67]
S	Bulk density	45	–	[74]
S	Bulk porosity	55	–	[156]
S	Bulk density	65.7	–	[58]
S, G	Apparent porosity	55	–	[88]
S, G	Bulk porosity	55	–	[87]

Appendix B: Supplementary Data for Fig. 10

Special treatment	Density or porosity type	Value (%)	Standard deviation (%)	Reference
–	Bulk density	35	–	[55]
–	Bulk density	38.4	–	[69]
–	Bulk density	48	–	[89]
–	Apparent porosity	46.07	8.52	[132]
–	Bulk density	55.89	–	[90]
–	Apparent porosity	41.42	4.35	[157]
–	Apparent solid density	65.2	–	[170]
–	Bulk porosity	32.1	2.6	[110]
–	Bulk porosity	32	–	[109]
C	Bulk density	55.3	–	[53]
C	Bulk porosity	12.9	0.5	[83]
G	Apparent solid density	32.2	–	[85]
G	Bulk density	38.78	3.64	[135]
G	Apparent porosity	59.43	–	[149]
G	Bulk density	42.95	1.6	[130]
G	Bulk density	43.2	–	[158]
G	Bulk density	48	–	[127]
G	Apparent solid density	48	–	[68]

Continued

Special treatment	Density or porosity type	Value (%)	Standard deviation (%)	Reference
G	Apparent porosity	51	0.9	[155]
G	Bulk density	62.5	–	[64]
G	Apparent porosity	36	–	[70]
G	Bulk density	67	–	[63]
G	Apparent solid density	91.4	2.8	[128]
I	Bulk density	85	–	[69]
L	Bulk density	99	–	[24]
L	Bulk density	99.9	–	[27]
M	Bulk porosity	65.3	–	[144]
M	Bulk porosity	44	–	[108]
M	Bulk density	66	–	[97]
M	Bulk density	72	2	[96]
M	Bulk density	94.5	–	[174]
P	Bulk density	60.1	–	[55]
P	Bulk density	94.33	–	[90]
S	Bulk density	65.5	2.4	[65]
S	Bulk porosity	30	–	[156]
S	Apparent solid density	96	–	[169]
G, I	Bulk porosity	19	0.5	[71]
G, I	Bulk density	91	–	[86]
G, I	Apparent porosity	2.4	–	[85]
G, P	Bulk density	97.8	–	[64]
G, S	Bulk density	86.8	–	[95]
I, C	Bulk density	55	–	[89]
M, G	Bulk density	45.06	3.05	[135]
M, G	Bulk density	52.84	2.76	[136]
M, G	Apparent solid density	95.1	4.72	[128]
M, G	Bulk density	95.74	–	[92]
M, G	Apparent porosity	2.5	0.12	[102]
M, G	Apparent solid density	99	0.1	[146]
M, L	Bulk porosity	8.79	1.44	[77]
M, L	Bulk density	99.2	–	[37]
M, S	Bulk density	54.8	–	[98]
M, G, P	Bulk density	99.2	–	[64]
M, G, C	Bulk porosity	48	2	[103]
M, G, I	Apparent porosity	1.7	–	[88]
M, L, P	Bulk density	100	–	[94]
M, S, G	Bulk density	53.01	–	[100]

Appendix C: Supplementary Data for Fig. 13

	Density before sintering			
Powder bed density (%)	Green density (%)	Pressed green density (%)	Density after sintering (%)	Reference
39.7	–	–	46.8	[65]
45.2	–	–	50.7	[65]
51	–	–	87.1	[83]
53	–	–	100	[94]
57.1	–	–	57.5	[65]
58.2	–	–	60.5	[65]
59.5	–	–	64.3	[65]
53.6	–	–	64.8	[65]
61.7	–	–	65.5	[65]
67	–	–	99	[24]
–	31	–	62.5	[64]
–	32	–	35	[55]
–	39	–	48	[89]
–	43.6	–	61.5	[63]
–	45	–	48	[68]
–	45	–	70	[156]
–	46.9	–	64.1	[63]
–	48	–	67	63]
–	57.2	–	99.2	[37]
–	58	–	99.9	[27]
–	–	47	87.9	[64]
–	–	54	95.9	[64]
–	–	56	97.8	[64]
–	–	61	99.2	[64]

References

[1] Klocke, F., 1997, "Modern Approaches for the Production of Ceramic Components," J. Eur. Ceram. Soc., **17**(2–3), pp. 457–465.
[2] Kremers, H. M., Larson, D. R., Crowson, C. S., Kremers, W. K., Washington, R. E., Steiner, C. A., Jiranek, W. A., and Berry, D. J., 2014, "Prevalence of Total Hip and Knee Replacement in the United States," J. Bone Jt. Surg. Am., **97**(17), pp. 1386–1397.
[3] Bose, S., and Tarafder, S., 2012, "Calcium Phosphate Ceramic Systems in Growth Factor and Drug Delivery for Bone Tissue Engineering: A Review," Acta Biomater., **8**(4), pp. 1401–1421.
[4] Gmeiner, R., Deisinger, U., Schönherr, J., Lechner, B., Detsch, R., Boccaccini, A. R., and Stampfl, J., 2015, "Additive Manufacturing of Bioactive Glasses and Silicate Bioceramics," J. Ceram. Sci. Technol., **6**(2), pp. 75–86.
[5] ASTM International, 2015, "*ISO/ASTM 52900:2015—Additive Manufacturing—General Principles—Terminology*," ASTM International, West Conshohocken, PA.
[6] Cima, M. J., Sachs, E., Fan, T., Michaels, S. P., Khanuja, S., Lauder, A., Lee, S.-J. J., Brancazio, D., Curodeau, A., and Tuerck, H., 1993, "Three-Dimensional Printing Techniques," Patent No. US5387380A.
[7] Sachs, E., Cima, M., and Cornie, J., 1990, "Three Dimensional Printing: Rapid Tooling and Prototypes Directly From CAD Representation," Solid Freeform Fabrication Symposium, Austin, TX, Aug. 6–8, pp. 27–47.
[8] Chua, C. K., and Leong, K. F., 2014, "3D Printing and Additive Manufacturing: Principles and Applications," World Scientific, Singapore.
[9] Chua, C. K., Leong, K. F., and Lim, C. S., 2010, "Rapid Prototyping: Principles and Applications," World Scientific, Singapore.
[10] Chua, C. K., Leong, K. F., and Lim, C. S., 2003, "Rapid Prototyping: Principles and Applications," World Scientific, Singapore.
[11] ExOne, "History | ExOne," https://www.exone.com/About-ExOne/History, Accessed February 9, 2019.
[12] Voxeljet, "Company History | Voxeljet 3D Printing Solutions," https://www.voxeljet.com/company/company-history/, Accessed February 9, 2019.
[13] MicroJet, "About MicroJet," http://www.microjet.com.tw/en/about/#. Accessed February 9, 2019.
[14] TCT Magazine, "Production Ready—Desktop Metal Prepares to Unleash Its Production System—TCT Magazine," https://www.tctmagazine.com/3d-printing-news/desktop-metal-unleashes-production-system/, Accessed February 9, 2019.
[15] TCT Magazine, "Digital Metal 3D Printing: The Smaller, the Better—TCT Magazine," https://www.tctmagazine.com/tct-events/tct-show-uk/digital-metal-metal-3d-printing-the-smaller-the-better/, Accessed February 10, 2019.
[16] Cima, M. J., and Sachs, E. M., 1991, "Three Dimensional Printing: Form, Materials, and Performance," Solid Freeform Fabrication Symposium, Austin, TX, Aug. 12–14, pp. 187–194.
[17] Cima, M., Lauder, A., Khanuja, S., and Sachs, E. M., 1992, "Microstructural Elements of Components Derived From 3D Printing," Solid Freeform Fabrication Symposium, Austin, TX, Aug. 3–5, pp. 220–227.
[18] Sachs, E., Cima, M., Williams, P., Brancazio, D., and Cornie, J., 1992, "Three Dimensional Printing: Rapid Tooling and Prototypes Directly From a CAD Model," J. Eng. Ind., **114**(4), pp. 481–488.
[19] Sachs, E., Cima, M., Cornie, J., Brancazio, D., Bredt, J., Curodeau, A., Fan, T., Khanuja, S., Lauder, A., Lee, J., and Michaels, S., 1993, "Three-Dimensional Printing: The Physics and Implications of Additive Manufacturing," CIRP Ann., **42**(1), pp. 257–260.
[20] Sachs, E. M., 2000, "Powder Dispensing Apparatus Using Vibration," US Patent No. US6036777A.
[21] Perrin, S. E., 1991, "Control of Thin Layer Powder Packing Density : Effects of Applied Vibration," Bachelor thesis, Massachusetts Institute of Technology, Cambridge, MA.
[22] Holman, R. K., Cima, M. J., Uhland, S. A., and Sachs, E., 2002, "Spreading and Infiltration of Inkjet-Printed Polymer Solution Droplets on a Porous Substrate," J. Colloid Interface Sci., **249**(2), pp. 432–440.
[23] Moon, J., Grau, J. E., Knezevic, V., Cima, M. J., and Sachs, E. M., 2002, "Ink-Jet Printing of Binders for Ceramic Components," J. Am. Ceram. Soc., **85**(4), pp. 755–762.
[24] Grau, J., Moon, J., Uhland, S., Cima, M., and Sachs, E., 1997, "High Green Density Ceramic Components Fabricated by the Slurry-Based 3DP Process," Solid Freeform Fabrication Symposium, Austin, TX, Aug. 11–13, pp. 371–379.
[25] Uhland, S. A., Holman, R. K., Cima, M. J., Sachs, E., and Enokido, Y., 1998, "New Process and Materials Developments in 3-Dimensional Printing, 3DP™," MRS Proceedings, Boston, MA, Apr. 13–15, pp. 153–158.
[26] Grau, J. E., 1998, "Fabrication of Engineered Ceramic Components by the Slurry-Based Three Dimensional Printing Process," PhD thesis, Massachusetts Institute of Technology, Cambridge, MA.
[27] Cima, M. J., Wang, H.-R., Cima, M. J., Oliveira, M., Wang, H. R., Sachs, E., and Holman, R., 2001, "Slurry-Based 3DP and Fine Ceramic Components," Solid Freeform Fabrication Symposium, Austin, TX, Aug. 6–8, pp. 216–223.
[28] Holman Richard, K., 2001, "Effects of the Polymeric Binder System in Slurry-Based Three Dimensional Printing of Ceramics," PhD thesis, Massachusetts Institute of Technology, Cambridge, MA.
[29] Wang, H. R., 2005, "Gradient-Index (GRIN) Lenses by Slurry-Based Three-Dimensional Printing (S-3DP)," PhD thesis, Massachusetts Institute of Technology, Cambridge, MA.
[30] Grau, J. E., Uhland, S. A., Moon, J., Cima, M. J., and Sachs, E. M., 2004, "Controlled Cracking of Multilayer Ceramic Bodies," J. Am. Ceram. Soc., **82**(8), pp. 2080–2086.
[31] Holman, R. K., Uhland, S. A., Cima, M. J., and Sachs, E., 2002, "Surface Adsorption Effects in the Inkjet Printing of an Aqueous Polymer Solution on a Porous Oxide Ceramic Substrate," J. Colloid Interface Sci., **247**(2), pp. 266–274.
[32] Lauder, A. J., 1992, "Microstructure and Particle Arrangement in Three Dimensional Printing," Master thesis, Massachusetts Institute of Technology, Cambridge, MA.
[33] Oliveira, M. A., 2002, "Slurry Based Three Dimensional Printing (S-3DP) of Tungsten Carbide Cobalt," PhD thesis, Massachusetts Institute of Technology, Cambridge, MA.
[34] Cima, M. J., Sachs, E. M., Cima, L. G., Yoo, J., Khanuja, S., Borland, S. W., Wu, B., and Giordano, R. A., 1994, "Computer-Derived Microstructures by 3D Printing: Bio-and Structural Materials," Solid Freeform Fabrication Symposium, Austin, TX, Aug. 8–10, pp. 181–190.
[35] Seitz, H., Rieder, W., Irsen, S., Leukers, B., and Tille, C., 2005, "Three-Dimensional Printing of Porous Ceramic Scaffolds for Bone Tissue Engineering," J. Biomed. Mater. Res., Part B, **74**(2), pp. 782–788.
[36] Du, W., Ren, X., Ma, C., and Pei, Z., 2017, "Binder Jetting Additive Manufacturing of Ceramics: A Literature Review," ASME 2017 International Mechanical Engineering Congress and Exposition, Tampa, FL, Nov. 5–8, pp. 1–12.
[37] Zocca, A., Lima, P., and Gunster, J., 2017, "LSD-Based 3D Printing of Alumina Ceramics," J. Ceram. Sci. Technol., **8**(1), pp. 141–148.
[38] Zocca, A., Colombo, P., Gomes, C. M., and Günster, J., 2015, "Additive Manufacturing of Ceramics: Issues, Potentialities, and Opportunities," J. Am. Ceram. Soc., **98**(7), pp. 1983–2001.
[39] Travitzky, N., Bonet, A., Dermeik, B., Fey, T., Filbert-Demut, I., Schlier, L., Schlordt, T., and Greil, P., 2014, "Additive Manufacturing of Ceramic-Based Materials," Adv. Eng. Mater., **16**(6), pp. 729–754.
[40] Jafari, M. A., Han, W., Mohammadi, F., Safari, A., Danforth, S. C., and Langrana, N., 2000, "A Novel System for Fused Deposition of Advanced Multiple Ceramics," Rapid Prototyp. J., **6**(3), pp. 161–175.
[41] Wang, F., Mei, J., Jiang, H., and Wu, X., 2007, "Laser Fabrication of Ti6Al4 V/TiC Composites Using Simultaneous Powder and Wire Feed," Mater. Sci. Eng. A, **445**, pp. 461–466.
[42] Balla, V. K., Bose, S., and Bandyopadhyay, A., 2008, "Processing of Bulk Alumina Ceramics Using Laser Engineered Net Shaping," Int. J. Appl. Ceram. Technol., **5**(3), pp. 234–242.
[43] Dong, C., 1990, "Binder Removal in Ceramics," PhD thesis, Massachusetts Institute of Technology, Cambridge, MA.
[44] Moon, J., Caballero, A. C., Hozer, L., Chiang, Y.-M., and Cima, M. J., 2001, "Fabrication of Functionally Graded Reaction Infiltrated SiC–Si Composite by Three-Dimensional Printing (3DP™) Process," Mater. Sci. Eng. A, **298**(1–2), pp. 110–119.
[45] Trombetta, R., Inzana, J. A., Schwarz, E. M., Kates, S. L., and Awad, H. A., 2017, "3D Printing of Calcium Phosphate Ceramics for Bone Tissue Engineering and Drug Delivery," Ann. Biomed. Eng., **45**(1), pp. 23–44.
[46] Tay, B. Y., Evans, J. R. G., and Edirisinghe, M. J., 2003, "Solid Freeform Fabrication of Ceramics," Int. Mater. Rev., **48**(6), pp. 341–370.
[47] Deckers, J., Vleugels, J., and Kruth, J. P., 2014, "Additive Manufacturing of Ceramics: A Review," J. Ceram. Sci. Technol., **5**(4), pp. 245–260.
[48] Yang, L., and Miyanaji, H., 2017, "Ceramic Additive Manufacturing: A Review of Current Status and Challenges," Solid Freeform Fabrication Symposium, Austin, TX, Aug. 7–9, pp. 652–679.
[49] Ziaee, M., and Crane, N. B., 2019, "Binder Jetting: A Review of Process, Materials, and Methods," Addit. Manuf., **28**, pp. 781–801.
[50] Moritz, T., and Maleksaeedi, S., 2018, "Additive Manufacturing of Ceramic Components," *Additive Manufacturing: Materials, Processes, Quantifications and Applications*, Butterworth-Heinemann, Oxford, pp. 105–161.
[51] Desktop Metal, "Production | Desktop Metal," https://www.desktopmetal.com/products/production/, Accessed February 10, 2019.
[52] Kang, S.-J. L., 2005, *Sintering : Densification, Grain Growth, and Microstructure*, Elsevier Butterworth-Heinemann, Burlington.
[53] Yao, D., Gomes, C. M., Zeng, Y. P., Jiang, D., Günster, J., and Heinrich, J. G., 2015, "Near Zero Shrinkage Porous Al2O3 Prepared via 3D-Printing and Reaction Bonding," Mater. Lett., **147**, pp. 116–118.
[54] Solis, D. M., Silva, A. V., Volpato, N., and Berti, L. F., 2019, "Reaction-Bonding of Aluminum Oxide Processed by Binder Jetting," J. Manuf. Processes, **41**, pp. 267–272.
[55] Díaz-Moreno, C. A., Lin, Y., Hurtado-Macías, A., Espalin, D., Terrazas, C. A., Murr, L. E., and Wicker, R. B., 2019, "Binder Jetting Additive Manufacturing of Aluminum Nitride Components," Ceram. Int., **45**(11), pp. 13620–13627.
[56] Diaz-Moreno, C. A., Rodarte, C., Ambriz, S., Bermudez, D., Roberson, D., Terrazas, C., Espalin, D., Ferguson, R., Shafirovich, E., Lin, Y., and Wicker, R. B., 2018, "Binder Jetting of High Temperature and Thermally Conductive (Aluminum Nitride) Ceramic," Solid Freeform Fabrication Symposium, Austin, TX, Aug. 13–15, pp. 143–159.
[57] Jimenez, E. M., Ding, D., Su, L., Joshi, A. R., Singh, A., Reeja-Jayan, B., and Beuth, J., 2019, "Parametric Analysis to Quantify Process Input Influence on the Printed Densities of Binder Jetted Alumina Ceramics," Addit. Manuf., **30**, p. 100864.
[58] Kunchala, P., and Kappagantula, K., 2018, "3D Printing High Density Ceramics Using Binder Jetting With Nanoparticle Densifiers," Mater. Des., **155**, pp. 443–450.
[59] Lanzetta, M., and Sachs, E., 2001, "The Line Formation With Alumina Powders in Drop on Demand Three Dimensional Printing," The First International

Seminar on Progress in Inovative Manufacturing Engineering, Sestri Levante, Italy, June 20–22, pp. 197–204.
[60] Lee, S. J. J., Sachs, E., and Cima, M., 1995, "Layer Position Accuracy in Powder-Based Rapid Prototyping," Rapid Prototyp. J., **1**(4), pp. 24–37.
[61] Sachs, E. M., Cima, M. J., Bredt, J. F., Curodeau, A., Fan, T., and Brancazio, D., 1992, "CAD-Casting: The Direct Fabrication of Ceramic Shells and Cores by Three-Dimensional Printing," Manuf. Rev., **5**(2), pp. 118–126.
[62] Sachs, E., Curodeau, A., Gossard, D., Jee, H., Cima, M., and Caldarise, S., 1994, "Surface Texture by 3D Printing," Solid Freeform Fabrication Symposium, Austin, TX, Aug. 8–10, pp. 56–64.
[63] Melcher, R., Travitzky, N., Zollfrank, C., and Greil, P., 2011, "3D Printing of Al2O3/Cu-O Interpenetrating Phase Composite," J. Mater. Sci., **46**(5), pp. 1203–1210.
[64] Yoo, J., Cima, M. J., Khanuja, S., and Sachs, E. M., 1993, "Structural Ceramic Components by 3D Printing," Solid Freeform Fabrication Symposium, Austin, TX, Aug. 9–11, pp. 40–50.
[65] Du, W., Ren, X., Chen, Y., Ma, C., Radovic, M., and Pei, Z., 2018, "Model Guided Mixing of Ceramic Powders With Graded Particle Sizes in Binder Jetting Additive Manufacturing," ASME 2018 13th International Manufacturing Science and Engineering Conference, College Station, TX, June 18–22, pp. 1–9.
[66] Du, W., Ren, X., Ma, C., and Pei, Z., 2019, "Ceramic Binder Jetting Additive Manufacturing: Particle Coating for Increasing Powder Sinterability and Part Strength," Mater. Lett., **234**, pp. 327–330.
[67] Hamano, R., and Ikoma, T., 2018, "Preparation of α-Alumina Powder and Binder For 3D Printer," MRS Adv., **3**(18), pp. 969–975.
[68] Hotta, M., Shimamura, A., Kondo, N., and Ohji, T., 2016, "Powder Layer Manufacturing of Alumina Ceramics Using Water Spray Bonding," J. Ceram. Soc. Japan, **124**(6), pp. 750–752.
[69] Maleksaeedi, S., Eng, H., Wiria, F. E., Ha, T. M. H., and He, Z., 2014, "Property Enhancement of 3D-Printed Alumina Ceramics Using Vacuum Infiltration," J. Mater. Process. Technol., **214**(7), pp. 1301–1306.
[70] Melcher, R., Martins, S., Travitzky, N., and Greil, P., 2006, "Fabrication of Al2O3-Based Composites by Indirect 3D-Printing," Mater. Lett., **60**(4), pp. 572–575.
[71] Zhang, W., Melcher, R., Travitzky, N., Bordia, R. K., and Greil, P., 2009, "Three-Dimensional Printing of Complex-Shaped Alumina/Glass Composites," Adv. Eng. Mater., **11**(12), pp. 1039–1043.
[72] Cima, M. J., Sachs, E. M., Cima, L. G., Yoo, J., Khanuja, S., Borland, S. W., Wu, B., and Giordano, R. A., 1994, "Computer-Derived Microstructures by 3D Printing: Bio- and Structural Materials," Solid Freeform Fabrication Symposium, Austin, TX, Aug. 8–10, pp. 181–190.
[73] Fleisher, A., Zolotaryov, D., Kovalevsky, A., Muller-Kamskii, G., Eshed, E., Kazakin, M., and Popov, V. V., 2019, "Reaction Bonding of Silicon Carbides by Binder Jet 3D-Printing, Phenolic Resin Binder Impregnation and Capillary Liquid Silicon Infiltration," Ceram. Int., **45**(14), pp. 18023–18029.
[74] Zhao, H., Ye, C., Fan, Z., and Wang, C., 2017, "3D Printing of CaO-Based Ceramic Core Using Nanozirconia Suspension as a Binder," J. Eur. Ceram. Soc., **37**(15), pp. 5119–5125.
[75] Budding, A., and Vaneker, T. H. J., 2013, "New Strategies for Powder Compaction in Powder-Based Rapid Prototyping Techniques," Procedia CIRP, **6**, pp. 527–532.
[76] Vaezi, M., and Chua, C. K., 2011, "Effects of Layer Thickness and Binder Saturation Level Parameters on 3D Printing Process," Int. J. Adv. Manuf. Technol., **53**(1–4), pp. 275–284.
[77] Lima, P., Zocca, A., Acchar, W., and Günster, J., 2018, "3D Printing of Porcelain by Layerwise Slurry Deposition," J. Eur. Ceram. Soc., **38**(9), pp. 3395–3400.
[78] Rabinskiy, L. N., Sitnikov, S. A., Pogodin, V. A., Ripetskiy, A. A., and Solyaev, Y. O., 2017, "Binder Jetting of Si3N4 Ceramics With Different Porosity," Solid State Phenom., **269**, pp. 37–50.
[79] Rabinskiy, L., Ripetsky, A., Sitnikov, S., Solyaev, Y., and Kahramanov, R., 2016, "Fabrication of Porous Silicon Nitride Ceramics Using Binder Jetting Technology," IOP Conf. Ser.: Mater. Sci. Eng., **140**(1), pp. 1–6.
[80] Fu, Z., Schlier, L., Travitzky, N., and Greil, P., 2013, "Three-Dimensional Printing of SiSiC Lattice Truss Structures," Mater. Sci. Eng. A, **560**, pp. 851–856.
[81] Zocca, A., Lima, P., Diener, S., Katsikis, N., and Günster, J., 2019, "Additive Manufacturing of SiSiC by Layerwise Slurry Deposition and Binder Jetting (LSD-Print)," J. Eur. Ceram. Soc., **39**(13), pp. 3527–3533.
[82] Travitzky, N., Zimmermann, K., Melcher, R., and Greil, P., 2006, "From Polysaccharides to SiSiC Composites by 3d Printing," Proceedings of the 107th Annual Meeting of the American Ceramic Society, Baltimore, MD, Apr. 10–13, pp. 37–45.
[83] Zocca, A., Gomes, C. M., Staude, A., Bernardo, E., Günster, J., and Colombo, P., 2013, "SiOC Ceramics With Ordered Porosity by 3D-Printing of a Preceramic Polymer," J. Mater. Res., **28**(17), pp. 2243–2252.
[84] Myers, K., Juhasz, M., Cortes, P., and Conner, B., 2015, "Mechanical Modeling Based on Numerical Homogenization of an Al2O3/Al Composite Manufactured via Binder Jet Printing," Comput. Mater. Sci., **108**, Part A, pp. 128–135.
[85] Nan, B., Yin, X., Zhang, L., and Cheng, L., 2011, "Three-Dimensional Printing of Ti3SiC2-Based Ceramics," J. Am. Ceram. Soc., **94**(4), pp. 969–972.
[86] Yin, X., Travitzky, N., Melcher, R., and Greil, P., 2006, "Three-Dimensional Printing of TiAl3/Al2O3 Composites," Zeitschrift für Met., **97**(5), pp. 492–498.
[87] Yin, X., Travitzky, N., and Greil, P., 2007, "Near-Net-Shape Fabrication of Ti3AlC2-Based Composites," Int. J. Appl. Ceram. Technol., **4**(2), pp. 184–190.
[88] Yin, X., Travitzky, N., and Greil, P., 2007, "Three-Dimensional Printing of Nanolaminated Ti3AlC2 Toughened TiAl3-Al2O3 Composites," J. Am. Ceram. Soc., **90**(7), pp. 2128–2134.
[89] Grant, L. O., Alameen, M. B., Carazzone, J. R., Fred, C., Iii, H., and Cordero, Z. C., 2018, "Mitigating Distortion During Sintering of Binder Jet Printed Ceramics," Solid Freeform Fabrication Symposium, Austin, TX, Aug. 13–15, pp. 135–142.
[90] Sun, W., Dcosta, D. J., Lin, F., and El-Raghy, T., 2002, "Freeform Fabrication of Ti3SiC2 Powder-Based Structures: Part I—Integrated Fabrication Process," J. Mater. Process. Technol., **127**(3), pp. 343–351.
[91] Dcosta, D. J., Sun, W., Lin, F., and Ei-Raghy, T., 2002, "Freeform Fabrication of Ti3SiC2 Powder-Based Structures: Part II—Characterization and Microstructure Evaluation," J. Mater. Process. Technol., **127**(3), pp. 352–360.
[92] Enneti, R. K., Prough, K. C., Wolfe, T. A., Klein, A., Studley, N., and Trasorras, J. L., 2018, "Sintering of WC-12%Co Processed by Binder Jet 3D Printing (BJ3DP) Technology," Int. J. Refract. Met. Hard Mater., **71**, pp. 28–35.
[93] Enneti, R. K., and Prough, K. C., 2019, "Wear Properties of Sintered WC-12% Co Processed via Binder Jet 3D Printing (BJ3DP)," Int. J. Refract. Met. Hard Mater., **78**, pp. 228–232.
[94] Kernan, B. D., Sachs, E. M., Oliveira, M. A., and Cima, M. J., 2007, "Three-Dimensional Printing of Tungsten Carbide–10 Wt% Cobalt Using a Cobalt Oxide Precursor," Int. J. Refract. Met. Hard Mater., **25**(1), pp. 82–94.
[95] Zhao, H., Ye, C., Fan, Z., and Shi, Y., 2015, "3D Printing of ZrO2 Ceramic Using Nano-Zirconia Suspension as a Binder," 4th International Conference on Sensors, Measurement and Intelligent Materials, Shenzhen, China, Dec. 27–28, pp. 654–657.
[96] Mancuso, E., Alharbi, N., Bretcanu, O. A., Marshall, M., Birch, M. A., McCaskie, A. W., and Dalgarno, K. W., 2017, "Three-Dimensional Printing of Porous Load-Bearing Bioceramic Scaffolds," Proc. Inst. Mech. Eng. Part H J. Eng. Med., **231**(6), pp. 575–585.
[97] Zocca, A., Gomes, C. M., Bernardo, E., Müller, R., Günster, J., and Colombo, P., 2013, "LAS Glass-Ceramic Scaffolds by Three-Dimensional Printing," J. Eur. Ceram. Soc., **33**(9), pp. 1525–1533.
[98] Sun, C., Tian, X., Wang, L., Liu, Y., Wirth, C. M., Günster, J., Li, D., and Jin, Z., 2017, "Effect of Particle Size Gradation on the Performance of Glass-Ceramic 3D Printing Process," Ceram. Int., **43**(1), pp. 578–584.
[99] Winkel, A., Meszaros, R., Reinsch, S., Müller, R., Travitzky, N., Fey, T., Greil, P., and Wondraczek, L., 2012, "Sintering of 3D-Printed Glass/HAp Composites," J. Am. Ceram. Soc., **95**(11), pp. 3387–3393.
[100] Seidenstuecker, M., Kerr, L., Bernstein, A., Mayr, H., Suedkamp, N., Gadow, R., Krieg, P., Hernandez Latorre, S., Thomann, R., Syrowatka, F., and Esslinger, S., 2017, "3D Powder Printed Bioglass and β-Tricalcium Phosphate Bone Scaffolds," Materials (Basel), **11**(13), pp. 1–21.
[101] Bergmann, C., Lindner, M., Zhang, W., Koczur, K., Kirsten, A., Telle, R., and Fischer, H., 2010, "3D Printing of Bone Substitute Implants Using Calcium Phosphate and Bioactive Glasses," J. Eur. Ceram. Soc., **30**(12), pp. 2563–2567.
[102] Suwanprateeb, J., Sanngam, R., Suvannapruk, W., and Panyathanmaporn, T., 2009, "Mechanical and In Vitro Performance of Apatite-Wollastonite Glass Ceramic Reinforced Hydroxyapatite Composite Fabricated by 3D-Printing," J. Mater. Sci. Mater. Med., **20**(6), pp. 1281–1289.
[103] Zocca, A., Elsayed, H., Bernardo, E., Gomes, C. M., Lopez-Heredia, M. A., Knabe, C., Colombo, P., and Günster, J., 2015, "3D-Printed Silicate Porous Bioceramics Using a Non-Sacrificial Preceramic Polymer Binder," Biofabrication, **7**(2), pp. 1–12.
[104] Komlev, V. S., Popov, V. K., Mironov, A. V., Fedotov, A. Y., Teterina, A. Y., Smirnov, I. V., Bozo, I. Y., Rybko, V. A., and Deev, R. V., 2015, "3D Printing of Octacalcium Phosphate Bone Substitutes," Front. Bioeng. Biotechnol., **3**, pp. 1–7.
[105] Szucs, T. D., and Brabazon, D., 2009, "Effect of Saturation and Post Processing on 3D Printed Calcium Phosphate Scaffolds," Bioceram. 21, **396–398**, pp. 663–666.
[106] Gildenhaar, R., Knabe, C., Gomes, C., Linow, U., Houshmand, A., and Berger, G., 2011, "Calcium Alkaline Phosphate Scaffolds for Bone Regeneration 3D-Fabricated by Additive Manufacturing," Key Eng. Mater., **493**, pp. 849–854.
[107] El-Ghannam, A., Cunningham, L., Pienkowski, D., and Hart, A., 2007, "Bone Engineering of the Rabbit Ulna," J. Oral Maxillofac. Surg., **65**(8), pp. 1495–1502.
[108] El-Ghannam, A., Hart, A., White, D., and Cunningham, L., 2013, "Mechanical Properties and Cytotoxicity of a Resorbable Bioactive Implant Prepared by Rapid Prototyping Technique," J. Biomed. Mater. Res. Part A, **101**(10), pp. 2851–2861.
[109] Shanjani, Y., Amritha De Croos, J. N., Pilliar, R. M., Kandel, R. A., and Toyserkani, E., 2010, "Solid Freeform Fabrication and Characterization of Porous Calcium Polyphosphate Structures for Tissue Engineering Purposes," J. Biomed. Mater. Res., Part B, **93**(2), pp. 510–519.
[110] Sheydaeian, E., Vlasea, M., Woo, A., Pilliar, R., Hu, E., and Toyserkani, E., 2017, "Effect of Glycerol Concentrations on the Mechanical Properties of Additive Manufactured Porous Calcium Polyphosphate Structures for Bone Substitute Applications," J. Biomed. Mater. Res., Part B, **105**(4), pp. 828–835.
[111] Butscher, A., Bohner, M., Roth, C., Ernstberger, A., Heuberger, R., Doebelin, N., Rudolf Von Rohr, P., and Müller, R., 2012, "Printability of Calcium Phosphate Powders for Three-Dimensional Printing of Tissue Engineering Scaffolds," Acta Biomater., **8**(1), pp. 373–385.
[112] Butscher, A., Bohner, M., Doebelin, N., Galea, L., Loeffel, O., and Müller, R., 2013, "Moisture Based Three-Dimensional Printing of Calcium Phosphate Structures for Scaffold Engineering," Acta Biomater., **9**(2), pp. 5369–5378.
[113] Mehrban, N., Bowen, J., Vorndran, E., Gbureck, U., and Grover, L. M., 2013, "Structural Changes to Resorbable Calcium Phosphate Bioceramic Aged In Vitro," Colloids Surf. B Biointerfaces, **111**, pp. 469–478.

[114] Peters, F., Groisman, D., Davids, R., Hänel, T., Dürr, H., and Klein, M., 2006, "Comparative Study of Patient Individual Implants From β-Tricalcium Phosphate Made by Different Techniques Based on CT Data," Materwiss. Werksttech., **37**(6), pp. 457–461.
[115] Becker, S. T., Bolte, H., Krapf, O., Seitz, H., Douglas, T., Sivananthan, S., Wiltfang, J., Sherry, E., and Warnke, P. H., 2009, "Endocultivation: 3D Printed Customized Porous Scaffolds for Heterotopic Bone Induction," Oral Oncol., **45**(11), pp. e181–e188.
[116] Klammert, U., Gbureck, U., Vorndran, E., Rödiger, J., Meyer-Marcotty, P., and Kübler, A. C., 2010, "3D Powder Printed Calcium Phosphate Implants for Reconstruction of Cranial and Maxillofacial Defects," J. Craniomaxillofac. Surg., **38**(8), pp. 565–570.
[117] Tamimi, F., Torres, J., Gbureck, U., Lopez-Cabarcos, E., Bassett, D. C., Alkhraisat, M. H., and Barralet, J. E., 2009, "Craniofacial Vertical Bone Augmentation: A Comparison Between 3D Printed Monolithic Monetite Blocks and Autologous Onlay Grafts in the Rabbit," Biomaterials, **30**(31), pp. 6318–6326.
[118] Tamimi, F., Torres, J., Al-Abedalla, K., Lopez-Cabarcos, E., Alkhraisat, M. H., Bassett, D. C., Gbureck, U., and Barralet, J. E., 2014, "Osseointegration of Dental Implants in 3D-Printed Synthetic Onlay Grafts Customized According to Bone Metabolic Activity in Recipient Site," Biomaterials, **35**(21), pp. 5436–5445.
[119] Torres, J., Tamimi, F., Alkhraisat, M. H., Prados-Frutos, J. C., Rastikerdar, E., Gbureck, U., Barralet, J. E., and López-Cabarcos, E., 2011, "Vertical Bone Augmentation With 3D-Synthetic Monetite Blocks in the Rabbit Calvaria," J. Clin. Periodontol., **38**(12), pp. 1147–1153.
[120] Gbureck, U., Hölzel, T., Klammert, U., Würzler, K., Müller, F. A., and Barralet, J. E., 2007, "Resorbable Dicalcium Phosphate Bone Substitutes Prepared by 3D Powder Printing," Adv. Funct. Mater., **17**(18), pp. 3940–3945.
[121] Castilho, M., Dias, M., Vorndran, E., Gbureck, U., Fernandes, P., Pires, I., Gouveia, B., Armés, H., Pires, E., and Rodrigues, J., 2014, "Application of a 3D Printed Customized Implant for Canine Cruciate Ligament Treatment by Tibial Tuberosity Advancement," Biofabrication, **6**(2), pp. 1–13.
[122] Habibovic, P., Gbureck, U., Doillon, C. J., Bassett, D. C., van Blitterswijk, C. A., and Barralet, J. E., 2008, "Osteoconduction and Osteoinduction of Low-Temperature 3D Printed Bioceramic Implants," Biomaterials, **29**(7), pp. 944–953.
[123] Gbureck, U., Hölzel, T., Doillon, C. J., Müller, F. A., and Barralet, J. E., 2007, "Direct Printing of Bioceramic Implants With Spatially Localized Angiogenic Factors," Adv. Mater., **19**(6), pp. 795–800.
[124] Vorndran, E., Klarner, M., Klammert, U., Grover, L. M., Patel, S., Barralet, J. E., and Gbureck, U., 2008, "3D Powder Printing of β-Tricalcium Phosphate Ceramics Using Different Strategies," Adv. Eng. Mater., **10**(12), pp. B67–B71.
[125] Klammert, U., Reuther, T., Jahn, C., Kraski, B., Kübler, A. C., and Gbureck, U., 2009, "Cytocompatibility of Brushite and Monetite Cell Culture Scaffolds Made by Three-Dimensional Powder Printing," Acta Biomater., **5**(2), pp. 727–734.
[126] Gbureck, U., Hölzel, T., Biermann, I., Barralet, J. E., and Grover, L. M., 2008, "Preparation of Tricalcium Phosphate/Calcium Pyrophosphate Structures via Rapid Prototyping," J. Mater. Sci. Mater. Med., **19**(4), pp. 1559–1563.
[127] Birkholz, M. N., Agrawal, G., Bergmann, C., Schröder, R., Lechner, S. J., Pich, A., and Fischer, H., 2015, "Calcium Phosphate/Microgel Composites for 3D Powderbed Printing of Ceramic Materials," Biomed. Tech., **61**(3), pp. 267–279.
[128] Fielding, G. A., Bandyopadhyay, A., and Bose, S., 2012, "Effects of Silica and Zinc Oxide Doping on Mechanical and Biological Properties of 3D Printed Tricalcium Phosphate Tissue Engineering Scaffolds," Dent. Mater., **28**(2), pp. 113–122.
[129] Warnke, P. H., Seitz, H., Warnke, F., Becker, S. T., Sivananthan, S., Sherry, E., Liu, Q., Wiltfang, J., and Douglas, T., 2010, "Ceramic Scaffolds Produced by Computer-Assisted 3D Printing and Sintering: Characterization and Biocompatibility Investigations," J. Biomed. Mater. Res., Part B, **93**(1), pp. 212–217.
[130] Tarafder, S., Balla, V. K., Davies, N. M., Bandyopadhyay, A., and Bose, S., 2013, "Microwave-Sintered 3D Printed Tricalcium Phosphate Scaffolds for Bone Tissue Engineering," J. Tissue Eng. Regen. Med., **7**(8), pp. 631–641.
[131] Igawa, K., Mochizuki, M., Sugimori, O., Shimizu, K., Yamazawa, K., Kawaguchi, H., Nakamura, K., Takato, T., Nishimura, R., Suzuki, S., Anzai, M., Chung, U.-I., and Sasaki, N., 2006, "Tailor-Made Tricalcium Phosphate Bone Implant Directly Fabricated by a Three-Dimensional Ink-Jet Printer," J. Artif. Organs, **9**(4), pp. 234–240.
[132] Santos, C. F. L., Silva, A. P., Lopes, L., Pires, I., and Correia, I. J., 2012, "Design and Production of Sintered β-Tricalcium Phosphate 3D Scaffolds for Bone Tissue Regeneration," Mater. Sci. Eng. C, **32**(5), pp. 1293–1298.
[133] Barralet, J., Gbureck, U., Habibovic, P., Vorndran, E., Gerard, C., and Doillon, C. J., 2009, "Angiogenesis in Calcium Phosphate Scaffolds by Inorganic Copper Ion Release," Tissue Eng. Part A, **15**(7), pp. 1601–1609.
[134] Roy, T. D., Simon, J. L., Ricci, J. L., Rekow, E. D., Thompson, V. P., and Parsons, J. R., 2003, "Performance of Degradable Composite Bone Repair Products Made via Three-Dimensional Fabrication Techniques," J. Biomed. Mater. Res., **66A**(2), pp. 283–291.
[135] Tarafder, S., Davies, N. M., Bandyopadhyay, A., and Bose, S., 2013, "3D Printed Tricalcium Phosphate Bone Tissue Engineering Scaffolds: Effect of SrO and MgO Doping on In Vivo Osteogenesis in a Rat Distal Femoral Defect Model," Biomater. Sci., **1**(12), pp. 1250–1259.
[136] Tarafder, S., Dernell, W. S., Bandyopadhyay, A., and Bose, S., 2015, "SrO- and MgO-Doped Microwave Sintered 3D Printed Tricalcium Phosphate Scaffolds: Mechanical Properties and In Vivo Osteogenesis in a Rabbit Model," J. Biomed. Mater. Res., Part B, **103**(3), pp. 679–690.
[137] Bose, S., Tarafder, S., and Bandyopadhyay, A., 2017, "Effect of Chemistry on Osteogenesis and Angiogenesis Towards Bone Tissue Engineering Using 3D Printed Scaffolds," Ann. Biomed. Eng., **45**(1), pp. 261–272.
[138] Castilho, M., Moseke, C., Ewald, A., Gbureck, U., Groll, J., Pires, I., Teßmar, J., and Vorndran, E., 2014, "Direct 3D Powder Printing of Biphasic Calcium Phosphate Scaffolds for Substitution of Complex Bone Defects," Biofabrication, **6**(1), pp. 1–12.
[139] Khalyfa, A., Vogt, S., Weisser, J., Grimm, G., Rechtenbach, A., Meyer, W., and Schnabelrauch, M., 2007, "Development of a New Calcium Phosphate Powder-Binder System for the 3D Printing of Patient Specific Implants," J. Mater. Sci. Mater. Med., **18**(5), pp. 909–916.
[140] Vella, J. B., Trombetta, R. P., Hoffman, M. D., Inzana, J., Awad, H., and Benoit, D. S. W., 2017, "Three Dimensional Printed Calcium Phosphate and Poly(Caprolactone) Composites With Improved Mechanical Properties and Preserved Microstructure," J. Biomed. Mater. Res. Part A, **106**(3), pp. 663–672.
[141] Inzana, J. A., Olvera, D., Fuller, S. M., Kelly, J. P., Graeve, O. A., Schwarz, E. M., Kates, S. L., and Awad, H. A., 2014, "3D Printing of Composite Calcium Phosphate and Collagen Scaffolds for Bone Regeneration," Biomaterials, **35**(13), pp. 4026–4034.
[142] Seitz, H., Deisinger, U., Leukers, B., Detsch, R., and Ziegler, G., 2009, "Different Calcium Phosphate Granules for 3-D Printing of Bone Tissue Engineering Scaffolds," Adv. Eng. Mater., **11**(5), pp. 41–46.
[143] Wang, Y., Wang, K., Li, X., Wei, Q., Chai, W., Wang, S., Che, Y., Lu, T., and Zhang, B., 2017, "3D Fabrication and Characterization of Phosphoric Acid Scaffold With a HA / β -TCP Weight Ratio of 60 : 40 for Bone Tissue Engineering Applications," PLoS One, **12**(4), pp. 1–17.
[144] Strobel, L., Rath, S., Maier, A., Beier, J., Arkudas, A., Greil, P., Horch, R., and Kneser, U., 2014, "Induction of Bone Formation in Biphasic Calcium Phosphate Scaffolds by Bone Morphogenetic Protein-2 and Primary Osteoblasts," J. Tissue Eng. Regen. Med., **8**(3), pp. 176–185.
[145] Rath, S. N., Strobel, L. A., Arkudas, A., Beier, J. P., Maier, A. K., Greil, P., Horch, R. E., and Kneser, U., 2012, "Osteoinduction and Survival of Osteoblasts and Bone-Marrow Stromal Cells in 3D Biphasic Calcium Phosphate Scaffolds Under Static and Dynamic Culture Conditions," J. Cell. Mol. Med., **16**(10), pp. 2350–2361.
[146] Detsch, R., Schaefer, S., Deisinger, U., Ziegler, G., Seitz, H., and Leukers, B., 2011, "In Vitro: Osteoclastic Activity Studies on Surfaces of 3D Printed Calcium Phosphate Scaffolds," J. Biomater. Appl., **26**(3), pp. 359–380.
[147] Zhou, Z., Buchanan, F., Mitchell, C., and Dunne, N., 2014, "Printability of Calcium Phosphate: Calcium Sulfate Powders for the Application of Tissue Engineered Bone Scaffolds Using the 3D Printing Technique," Mater. Sci. Eng. C, **38**(1), pp. 1–10.
[148] Spath, S., Drescher, P., and Seitz, H., 2015, "Impact of Particle Size of Ceramic Granule Blends on Mechanical Strength and Porosity of 3D Printed Scaffolds," Materials (Basel), **8**(8), pp. 4720–4732.
[149] Chumnanklang, R., Panyathanmaporn, T., Sitthiseripratip, K., and Suwanprateeb, J., 2007, "3D Printing of Hydroxyapatite: Effect of Binder Concentration in Pre-Coated Particle on Part Strength," Mater. Sci. Eng. C, **27**(4), pp. 914–921.
[150] Wang, Y., Li, X., Li, C., Yang, M., and Wei, Q., 2015, "Binder Droplet Impact Mechanism on a Hydroxyapatite Microsphere Surface in 3D Printing of Bone Scaffolds," J. Mater. Sci., **50**(14), pp. 5014–5023.
[151] Spath, S., and Seitz, H., 2014, "Influence of Grain Size and Grain-Size Distribution on Workability of Granules With 3D Printing," Int. J. Adv. Manuf. Technol., **70**(1–4), pp. 135–144.
[152] Fierz, F. C., Beckmann, F., Huser, M., Irsen, S. H., Leukers, B., Witte, F., Degistirici, Ö, Andronache, A., Thie, M., and Müller, B., 2008, "The Morphology of Anisotropic 3D-Printed Hydroxyapatite Scaffolds," Biomaterials, **29**(28), pp. 3799–3806.
[153] Irsen, S. H., Leukers, B., Höckling, C., Tille, C., and Seitz, H., 2006, "Bioceramic Granulates for Use in 3D Printing: Process Engineering Aspects," Materwiss. Werksttech., **37**(6), pp. 533–537.
[154] Leukers, B., Gülkan, H., Irsen, S., Milz, S., Tille, C., Schieker, M., and Seitz, H., 2005, "Hydroxyapatite Scaffolds for Bone Tissue Engineering Made by 3D Printing," J. Mater. Sci. Mater. Med., **6**(12), pp. 1121–1124.
[155] Suwanprateeb, J., Sanngam, R., and Panyathanmaporn, T., 2010, "Influence of Raw Powder Preparation Routes on Properties of Hydroxyapatite Fabricated by 3D Printing Technique," Mater. Sci. Eng. C, **30**(4), pp. 610–617.
[156] Will, J., Melcher, R., Treul, C., Travitzky, N., Kneser, U., Polykandriotis, E., Horch, R., and Greil, P., 2008, "Porous Ceramic Bone Scaffolds for Vascularized Bone Tissue Regeneration," J. Mater. Sci. Mater. Med., **19**(8), pp. 2781–2790.
[157] Qian, C., and Sun, J., 2013, "Fabrication of the Porous Hydroxyapatite Implant by 3D Printing," J. Ceram. Process. Res., **14**(4), pp. 513–516.
[158] Suwanprateeb, J., Sanngam, R., and Suwanpreuk, W., 2008, "Fabrication of Bioactive Hydroxyapatite/Bis-GMA Based Composite via Three Dimensional Printing," J. Mater. Sci. Mater. Med., **19**(7), pp. 2637–2645.
[159] Farzadi, A., Solati-Hashjin, M., Asadi-Eydivand, M., and Osman, N. A. A., 2014, "Effect of Layer Thickness and Printing Orientation on Mechanical Properties and Dimensional Accuracy of 3D Printed Porous Samples for Bone Tissue Engineering," PLoS One, **9**(9), pp. 1–14.
[160] Farzadi, A., Waran, V., Solati-Hashjin, M., Rahman, Z. A. A., Asadi, M., and Osman, N. A. A., 2015, "Effect of Layer Printing Delay on Mechanical Properties and Dimensional Accuracy of 3D Printed Porous Prototypes in Bone Tissue Engineering," Ceram. Int., **41**(7), pp. 8320–8330.
[161] Asadi-Eydivand, M., Solati-Hashjin, M., Fathi, A., Padashi, M., and Abu Osman, N. A., 2016, "Optimal Design of a 3D-Printed Scaffold Using Intelligent Evolutionary Algorithms," Appl. Soft Comput. J., **39**, pp. 36–47.
[162] Suwanprateeb, J., Thammarakcharoen, F., and Hobang, N., 2016, "Enhancement of Mechanical Properties of 3D Printed Hydroxyapatite by

Combined Low and High Molecular Weight Polycaprolactone Sequential Infiltration," J. Mater. Sci. Mater. Med., **27**(11), pp. 1–12.
[163] Suwanprateeb, J., Thammarakcharoen, F., Wasoontararat, K., and Suvannapruk, W., 2012, "Influence of Printing Parameters on the Transformation Efficiency of 3D-Printed Plaster of Paris to Hydroxyapatite and Its Properties," Rapid Prototyp. J., **18**(6), pp. 490–499.
[164] Lowmunkong, R., Sohmura, T., Suzuki, Y., Matsuya, S., and Ishikawa, K., 2009, "Fabrication of Freeform Bone-Filling Calcium Phosphate Ceramics by Gypsum 3D Printing Method," J. Biomed. Mater. Res., Part B, **90 B**(2), pp. 531–539.
[165] Zhou, Z., Mitchell, C. A., Buchanan, F. J., and Dunne, N. J., 2013, "Effects of Heat Treatment on the Mechanical and Degradation Properties of 3D-Printed Calcium-Sulphate-Based Scaffolds," ISRN Biomater., **2013**, pp. 1–10.
[166] Suvannapruk, W., Thammarakcharoen, F., Phanpiriya, P., and Suwanprateeb, J., 2013, "Development of Antibiotics Impregnated Nanosized Silver Phosphate-Doped Hydroxyapatite Bone Graft," J. Nanomater., **2013**, pp. 1–9.
[167] Meininger, S., Mandal, S., Kumar, A., Groll, J., Basu, B., and Gbureck, U., 2016, "Strength Reliability and In Vitro Degradation of Three-Dimensional Powder Printed Strontium-Substituted Magnesium Phosphate Scaffolds," Acta Biomater., **31**, pp. 401–411.
[168] Klammert, U., Vorndran, E., Reuther, T., Müller, F. A., Zorn, K., and Gbureck, U., 2010, "Low Temperature Fabrication of Magnesium Phosphate Cement Scaffolds by 3D Powder Printing," J. Mater. Sci. Mater. Med., **21**(11), pp. 2947–2953.
[169] Gonzalez, J. A., Mireles, J., Lin, Y., and Wicker, R. B., 2016, "Characterization of Ceramic Components Fabricated Using Binder Jetting Additive Manufacturing Technology," Ceram. Int., **42**(9), pp. 10559–10564.
[170] Gaytan, S. M., Cadena, M. A., Karim, H., Delfin, D., Lin, Y., Espalin, D., MacDonald, E., and Wicker, R. B., 2015, "Fabrication of Barium Titanate by Binder Jetting Additive Manufacturing Technology," Ceram. Int., **41**(5), pp. 6610–6619.
[171] Gaytan, S. M., Cadena, M., Aldaz, M., Herderick, E., Medina, F., Wicker, R., and Keck, W. M., 2013, "Analysis of Ferroelectric Ceramic Fabricated by Binder Jetting Technology," Solid Freeform Fabrication Symposium, Austin, Aug. 12–14, pp. 859–868.
[172] Utela, B., Anderson, R. L., and Kuhn, H., 2006, "Advanced Ceramic Materials and Processes for Three-Dimensional Printing (3DP)," Solid Freeform Fabrication Symposium, Austin, TX, Aug. 14–16, pp. 290–303.
[173] Miyanaji, H., Zhang, S., Lassell, A., Zandinejad, A. A., and Yang, L., 2016, "Optimal Process Parameters for 3D Printing of Porcelain Structures," Procedia Manuf., **5**, pp. 870–887.
[174] Miyanaji, H., Zhang, S., Lassell, A., Zandinejad, A., and Yang, L., 2016, "Process Development of Porcelain Ceramic Material With Binder Jetting Process for Dental Applications," JOM, **68**(3), pp. 831–841.
[175] Miyanaji, H., Yang, L., Zhang, S., and Zandinejad, A., 2014, "A Preliminary Study of the Graded Dental Porcelain Ceramic Structures Fabricated via Binder Jetting 3D Printing," Solid Freeform Fabrication Symposium, Austin, TX, Aug. 4–6, pp. 578–589.
[176] Wang, H.-R., Cima, M. J., and Sachs, E. M., 2002, "Three-Dimensional Printing (3DP™) of Gradient-Index (GRIN) Lenses," Proceedings of the Innovative Processing and Synthesis of Ceramics, Glasses and Composites, St. Louis, MO, Apr. 28–May 1, pp. 191–201.
[177] Kumar, A., Nune, K. C., Murr, L. E., and Misra, R. D. K., 2016, "Biocompatibility and Mechanical Behaviour of Three-Dimensional Scaffolds for Biomedical Devices: Process–Structure–Property Paradigm," Int. Mater. Rev., **61**(1), pp. 20–45.
[178] Hsu, T., and Lai, W., 2010, "Manufacturing Parts Optimization in the Three-Dimensional Printing Process by the Taguchi Method," J. Chinese Inst. Eng., **33**(1), pp. 121–130.
[179] Butscher, A., Bohner, M., Hofmann, S., Gauckler, L., and Müller, R., 2011, "Structural and Material Approaches to Bone Tissue Engineering in Powder-Based Three-Dimensional Printing," Acta Biomater., **7**(3), pp. 907–920.
[180] Utela, B., Storti, D., Anderson, R., and Ganter, M., 2008, "A Review of Process Development Steps for New Material Systems in Three Dimensional Printing (3DP)," J. Manuf. Processes, **10**(2), pp. 96–104.
[181] ASTM International, 2015, "*B527-15: Standard Test Method for Tap Density of Metal Powders and Compounds*," ASTM International, West Conshohocken, PA.
[182] ISO, 2011, "ISO 3953:2011 Metallic Powders—Determination of Tap Density."
[183] German, R. M., 2014, *Sintering : From Empirical Observations to Scientific Principles*, Butterworth-Heinemann, Oxford, UK.
[184] Hwang, H. J., Yasuoka, M., Sando, M., Toriyama, M., and Niihara, K., 1999, "Fabrication, Sinterability, and Mechanical Properties of Lead Zirconate Titanate/Silver Composites," J. Am. Ceram. Soc., **82**(9), pp. 2417–2422.
[185] Saboori, A., Novara, C., Pavese, M., Badini, C., Giorgis, F., and Fino, P., 2017, "An Investigation on the Sinterability and the Compaction Behavior of Aluminum/Graphene Nanoplatelets (GNPs) Prepared by Powder Metallurgy," J. Mater. Eng. Perform., **26**(3), pp. 993–999.
[186] Callister, W. D., and Rethwisch, D. G., 2009, *Materials Science and Engineering: An Introduction*, Wiley, Danvers.
[187] Cho, G.-C., Dodds, J., and Santamarina, J. C., 2006, "Particle Shape Effects on Packing Density, Stiffness, and Strength: Natural and Crushed Sands," J. Geotech. Geoenvironmental Eng., **132**(5), pp. 591–602.
[188] Yu, A. B., Bridgwater, J., and Burbidge, A., 1997, "On the Modelling of the Packing of Fine Particles," Powder Technol., **92**(3), pp. 185–194.
[189] Cai, K., Román-Manso, B., Smay, J. E., Zhou, J., Osendi, M. I., Belmonte, M., and Miranzo, P., 2012, "Geometrically Complex Silicon Carbide Structures Fabricated by Robocasting," J. Am. Ceram. Soc., **95**(8), pp. 2660–2666.
[190] Haeri, S., Wang, Y., Ghita, O., and Sun, J., 2017, "Discrete Element Simulation and Experimental Study of Powder Spreading Process in Additive Manufacturing," Powder Technol., **306**, pp. 45–54.
[191] Shanjani, Y., and Ehsan, T., 2008, "Material Spreading and Compaction in Powder-Based Solid Freeform Fabrication Methods: Mathematical Modeling," Solid Freeform Fabrication Symposium, Austin, TX, Aug. 4–6.
[192] Roy, N. K., and Cullinan, M. A., 2015, "-SLS of Metals: Design of the Powder Spreader, Powder Bed Actuators and Optics for the System," Solid Freeform Fabrication Symposium, Austin, TX, Aug. 10–12, pp. 134–155.
[193] Apelt, D., Theiss, F., El-Warrak, A. O., Zlinszky, K., Bettschart-Wolfisberger, R., Bohner, M., Matter, S., Auer, J. A., and Von Rechenberg, B., 2004, "In Vivo Behavior of Three Different Injectable Hydraulic Calcium Phosphate Cements," Biomaterials, **25**(7–8), pp. 1439–1451.
[194] Bredt, J. F., Anderson, T. C., and Russell, D. B., 2006, "Three Dimensional Printing Material System and Method," US Patent No. US7087109B2.
[195] Vacanti, J. P., Cima, L. G., and Cima, M. J., 2001, "Vascularized Tissue Regeneration Matrices Formed By Solid Free Form Fabrication Techniques," US Patent No. US6176874B1.
[196] Meier, C., Weissbach, R., Weinberg, J., Wall, W. A., and Hart, A. J., 2019, "Critical Influences of Particle Size and Adhesion on the Powder Layer Uniformity in Metal Additive Manufacturing," J. Mater. Process. Technol., **266**, pp. 484–501.
[197] Katashinskii, V. P., and Shtern, M. B., 1983, "Stressed-Strained State of Powder Being Rolled in the Densification Zone. I. Mathematical Model of Rolling in the Densification Zone," Sov. Powder Metall. Met. Ceram., **22**(11), pp. 882–885.
[198] Jenni, M., Schimmer, L., and Zauner, R., 2008, "Quantitative Study of Powder Binder Separation of Feedstocks," PIM Int., **2**(4), pp. 50–55.
[199] ASTM International, 2013, "B212-13: Standard Test Method for Apparent Density of Free-Flowing Metal Powders Using the Hall Flowmeter Funnel," ASTM International, West Conshohocken, PA.
[200] ASTM International, 2014, "B329-14: Standard Test Method for Apparent Density of Metal Powders and Compounds Using the Scott Volumeter," ASTM International, West Conshohocken, PA.
[201] ASTM International, 2013, "B417 2013: Standard Test Method for Apparent Density of Non-Free-Flowing Metal Powders Using the Carney Funnel," ASTM International, West Conshohocken, PA.
[202] ASTM International, 2014, "B703-10: Standard Test Method for Apparent Density of Metal Powders and Related Compounds Using the Arnold Meter," ASTM International, West Conshohocken, PA.
[203] Elliott, A. M., Nandwana, P., Siddel, D., and Compton, B. G., 2016, "A Method for Measuring Powder Bed Density in Binder Jet Additive Manufacturing Process and the Powder Feedstock Characteristics Influencing the Powder Bed Density," Solid Freeform Fabrication Symposium, Austin, TX, Aug. 8–10, pp. 1031–1037.
[204] ISO, 2013, "ISO 18754:2013 Fine Ceramics (Advanced Ceramics, Advanced Technical Ceramics)—Determination of Density and Apparent Porosity."
[205] ASTM International, 2015, "*C20-00: Standard Test Methods for Apparent Porosity, Water Absorption, Apparent Specific Gravity, and Bulk Density of Burned Refractory Brick and Shapes by Boiling Water*," ASTM International, West Conshohocken, PA.
[206] ASTM International, 2017, "C373-17: Standard Test Methods for Water Absorption and Associate Properties by Vacuum Method for Pressed Ceramic Tiles," ASTM International, West Conshohocken, PA.
[207] ASTM International, 2017, "B962-17: Standard Test Methods for Density of Compacted or Sintered Powder Metallurgy (PM) Products Using Archimedes' Principle," ASTM International, West Conshohocken, PA.
[208] Abell, A. B., Willis, K. L., and Lange, D. A., 1999, "Mercury Intrusion Porosimetry and Image Analysis of Cement-Based Materials," J. Colloid Interface Sci., **211**(1), pp. 39–44.
[209] Tamari, S., 2004, "Optimum Design of the Constant-Volume Gas Pycnometer for Determining the Volume of Solid Particles," Meas. Sci. Technol., **15**(3), pp. 549–558.
[210] Sinka, I. C., Burch, S. F., Tweed, J. H., and Cunningham, J. C., 2004, "Measurement of Density Variations in Tablets Using X-Ray Computed Tomography," Int. J. Pharm., **271**(1–2), pp. 215–224.
[211] Rahaman, M. N., 2003, *Ceramic Processing and Sintering*, Marcel Dekker, New York.
[212] Morikawa, H., Minato, I., Tomita, T., and Iwai, S., 1975, "Anhydrite: A Refinement," Acta Crystallogr., **B31**(8), pp. 2164–2165.
[213] Wang, P. Y., Li, H. J., Qi, L. H., Zeng, X. H., and Zuo, H. S., 2011, "Synthesis of Al-TiAl3compound by Reactive Deposition of Molten Al Droplets and Ti Powders," Prog. Nat. Sci., **21**(2), pp. 153–158.
[214] Yang, R. Y., Zou, R. P., and Yu, A. B., 2000, "Computer Simulation of the Packing of Fine Particles," Phys. Rev. E, **62**(3), pp. 3900–3908.
[215] Litster, J. D., and Ennis, B. J., 2004, *The Science and Engineering of Granulation Process*, Springer Science, Dordrecht.
[216] Ma, C., Pei, Z., Ren, X., and Du, W., 2019, "Hierarchical Compositions for the Additive Manufacturing of Materials," US Patent No. US 2019/0111585 A1.
[217] Stuer, M., Zhao, Z., and Bowen, P., 2012, "Freeze Granulation: Powder Processing for Transparent Alumina Applications," J. Eur. Ceram. Soc., **32**(11), pp. 2899–2908.
[218] Saluja, V., Amorij, J. P., Kapteyn, J. C., de Boer, A. H., Frijlink, H. W., and Hinrichs, W. L. J., 2010, "A Comparison Between Spray Drying and Spray Freeze Drying to Produce an Influenza Subunit Vaccine Powder for Inhalation," J. Controlled Release, **144**(2), pp. 127–133.
[219] Du, W., Miao, G., Liu, L., Pei, Z., and Ma, C., 2019, "Binder Jetting Additive Manufacturing of Ceramics: Feedstock Powder Preparation by Spray Freeze

Granulation," ASME 2019 14th International Manufacturing Science and Engineering Conference, Errie, PA, June 10–14, pp. 1–6.
[220] Du, W., Miao, G., Liu, L., Pei, Z., and Ma, C., 2019, "Binder Jetting Additive Manufacturing of Ceramics: Comparison of Flowability and Sinterability Between Raw and Granulated Powders," ASME 2019 14th International Manufacturing Science and Engineering Conference, American Society of Mechanical Engineers, Errie, PA, June 10–14, pp. 1–8.
[221] Stovall, T., de Larrard, F., and Buil, M., 1986, "Linear Packing Density Model of Grain Mixtures," Powder Technol., **48**(1), pp. 1–12.
[222] Mühler, T., Gomes, C. M., Heinrich, J., and Günster, J., 2015, "Slurry-Based Additive Manufacturing of Ceramics," Int. J. Appl. Ceram. Technol., **12**(1), pp. 18–25.
[223] Hu, K., Wei, Y., Lu, Z., Wan, L., and Li, P., 2018, "Design of a Shaping System for Stereolithography With High Solid Loading Ceramic Suspensions," 3D Print. Addit. Manuf., **5**(4), pp. 311–318.
[224] Mamatha, S., Biswas, P., Ramavath, P., Das, D., and Johnson, R., 2018, "3D Printing of Complex Shaped Alumina Parts," Ceram. Int., **44**(16), pp. 19278–19281.
[225] Breval, E., Cheng, J. P., Agrawal, D. K., Gigl, P., Dennis, M., Roy, R., and Papworth, A. J., 2005, "Comparison Between Microwave and Conventional Sintering of WC/Co Composites," Mater. Sci. Eng. A, **391**(1–2), pp. 285–295.
[226] Rahaman, M. N., 2003, *Ceramic Processing and Sintering*, CRC Press, New York.
[227] Barsoum, M. W., 2002, *Fundamentals of Ceramics*, CRC Press, New York.
[228] Kang, S.-J. L., 2005, *Sintering: Densification, Grain Growth, and Microstructure*, Elsevier Butterworth-Heinemann, Burlington.
[229] Ainsley, C., and Gong, H., 1999, "Precision Sintering of Slip Cast Components," J. Mater. Process. Technol., **95**(1–3), pp. 201–209.
[230] Vermeiren, E., 2002, "The Advantages of All-Round Pressure," Met. Powder Rep., **57**(2), pp. 18–21.
[231] Koizumi, M., and Nishihara, M., 1991, *Isostatic Pressing: Technology and Applications*, Springer Science & Business Media, New York.
[232] Balakrishnan, A., Pizette, P., Martin, C. L., Joshi, S. V., and Saha, B. P., 2010, "Effect of Particle Size in Aggregated and Agglomerated Ceramic Powders," Acta Mater., **58**(3), pp. 802–812.
[233] Boltachev, G. S., and Volkov, N. B., 2010, "Size Effect in Nanopowder Compaction," Tech. Phys. Lett., **36**(9), pp. 823–826.
[234] ExOne, "ExOne | ACT Whitepaper," https://www.exone.com/en-US/ExOne-Triple-ACT-Whitepaper, Accessed January 18, 2020